Aus dem Institut für Physik der Universität Potsdam
Arbeitsgruppe Nichtlineare Dynamik

Dusty Ringlets In Saturn's Ring System

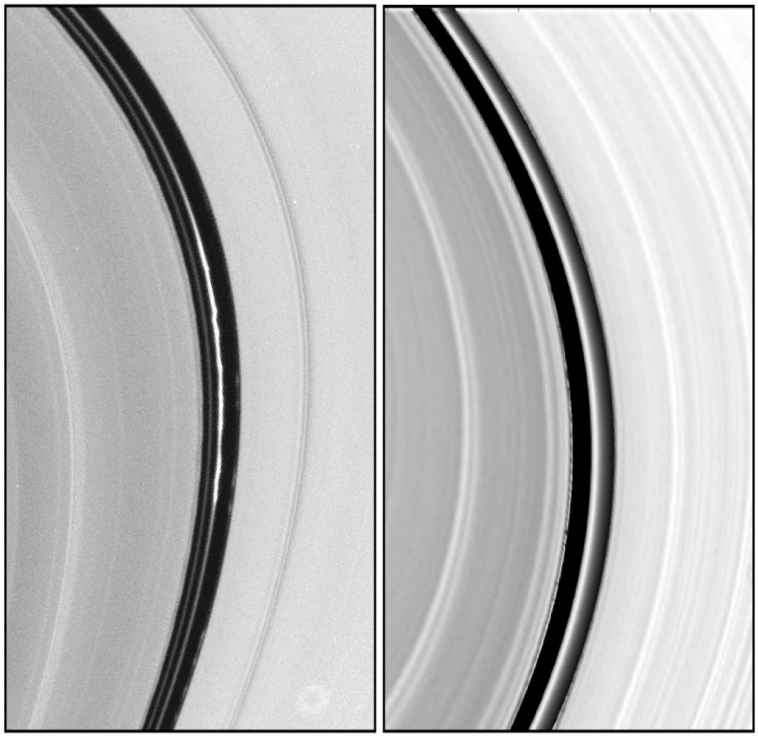

Diplomarbeit im Studiengang Diplom-Physik
vorgelegt von:

Robert Johann Flassig[⋆]

Betreuender Gutachter: Prof. Dr. Frank Spahn

Zweiter Gutachter: Prof. Dr. Arkady Pikovsky

Universität Potsdam, 22. September 2008

[⋆] flassig@agnld.uni-potsdam.de

Online published at the
Institutional Repository of the Potsdam University:
http://opus.kobv.de/ubp/volltexte/2008/2704/
urn:nbn:de:kobv:517-opus-27046
[http://nbn-resolving.de/urn:nbn:de:kobv:517-opus-27046]

Abstract

Recently, several faint ringlets in the Saturnian ring system were found to maintain a peculiar orientation relative to Sun. The Encke gap ringlets as well as the ringlet in the outer rift of the Cassini division were found to have distinct spatial displacements of several tens of kilometers away from Saturn towards Sun, referred to as *heliotropicity* (Hedman et al., 2007). This is quite exceptional, since dynamically one would expect eccentric features in the Saturnian rings to precess around Saturn over periods of months.

In our study we address this exceptional behavior by investigating the dynamics of circumplanetary dust particles with sizes in the range of 1-100 μm. These small particles are perturbed by non-gravitational forces, in particular, solar radiation pressure, Lorentz force, and planetary oblateness, on time-scales of the order of days. The combined influences of these forces cause periodical evolutions of grains' orbital eccentricities as well as precession of their pericenters, which can be shown by secular perturbation theory. We show that this interaction results in a stationary eccentric ringlet, oriented with its apocenter towards the Sun, which is consistent with observational findings.

By applying this heliotropic dynamics to the central Encke gap ringlet, we can give a limit for the expected smallest grain size in the ringlet of about 8.7 microns, and constrain the minimal lifetime to lie in the order of months. Furthermore, our model matches fairly well the observed ringlet eccentricity in the Encke gap, which supports recent estimates on the size distribution of the ringlet material (Hedman et al., 2007).

The ringlet-width however, that results from our modeling based on heliotropic dynamics, slightly overestimates the observed confined ringlet-width by a factor of 3 to 10, depending on the width-measure being used. This is indicative for mechanisms, not included in the heliotropic model, which potentially confine the ringlet to its observed width, including shepherding and scattering by embedded moonlets in the ringlet region.

Based on these results, early investigations (Cuzzi et al., 1984, Spahn and Wiebicke,

1989, Spahn and Sponholz, 1989), and recent work that has been published on the F ring (Murray et al., 2008) - to which the Encke gap ringlets are found to share similar morphological structures - we model the maintenance of the central ringlet by embedded moonlets. These moonlets, believed to have sizes of hundreds of meters across, release material into space, which is eroded by micrometeoroid bombardment (Divine, 1993).

We further argue that *Pan* - one of Saturn's moons, which shares its orbit with the central ringlet of the Encke gap - is a rather weak source of ringlet material that efficiently confines the ringlet sources (moonlets) to move on horseshoe-like orbits. Moreover, we suppose that most of the narrow heliotropic ringlets are fed by a moonlet population, which is held together by the largest member to move on horseshoe-like orbits. Modeling the equilibrium between particle source and sinks with a primitive balance equation based on photometric observations (Porco et al., 2005), we find the minimal effective source mass of the order of $3 \cdot 10^{-2} M_{\mathrm{Pan}}$, which is needed to keep the central ringlet from disappearing.

The cover shows the outer part of Saturn's A ring, including the Encke gap with its central and inner (only in the left image) dusty ringlets. The right image is composed out of an A ring image and the central ringlet produced by the annulus model derived in this study. Notice the circular distortion in the lower right corner of left image, which is due to an impact of a small particle onto the lens. Both images were taken by Cassini in 2004 (Credit: ciclops.org).

Acknowledgements

Thanks go to my supervisor F. Spahn and colleagues A. H. Guimaraes, E. Jamrath, E. V. Neto, M. Makuch, J. Schmidt, M. Seiß, and K.-U. Thiessenhusen for their motivated guidance in introducing me to scientific work, especially on such a nice topic. Thanks for your enormous support in various kinds of way. I also acknowledge the unique spirit of this special group.

Substantial life support - socially as well as financially - came from my parents Christine and Michael F., which I acknowledge hereby. Also not to forget about my dear brother Peter F., I am grateful for every minute we spend together!

I express thanks to my band mate Rainer B.- a.k.a. Grandmaster B - for such good times we have with our band project *Erntefest*.

There are many other personalities and materials, including the coffee farmers in Central America as well as the paper from spruces and pines, that have contributions to this work. Thank you all.

Finally, my dear darling Sara, thanks for being around.

Contents

CHAPTER 1

Introduction

Uniqueness in any sense has fascinated human perception of the universe since the early days of our existence. Creamy, white colored clouds on blue sky embellished by sunlight that scatters its way through the air. At night, the moon and its various forms of appearance, as well as the stars and the mystique tone that comes with them. These sorts of impressions have been - still are and will always be - the main source of questioning. The journey of search has brought us a long way on such a diverse field of investigations. This diploma thesis humbly tries to give a contribution to the understanding of solar system dynamics, with focus on structure formation in planetary rings.

Since mankind has risen on Earth, celestial bodies have been observed during clear night sky. Primitively in the beginning by naked eye, and mostly motivated by religious and cultural interests, observations have continuously advanced in two senses. First being more scientifically motivated and second technically more advanced. In 1610, Galileo Galilei discovered Saturn's rings with an ordinary telescope. By that time, the rings were thought to be moons, until 45 years later, Huygens correctly identified them as rings. In the mid to late 70s, the two Pioneer spacecraft marked a new era of space exploration. A major progress in understanding planetary rings came with Voyager spacecrafts in the early 80's. Their detectors, capable of detecting a wide range of wave length and resolution, supplied fabulous material. Voyager 1/2 have pushed planetary ring knowledge to an yet unreached level. On top of that, the spacecraft Cassini has been launched on its way to Saturn and arrived its insertion orbit on July 1, 2004. Since then, an unbelievable amount of valuable data has been collected, which has revealed tremendous properties of Saturn's ring system. By now, Cassini is on its first extended mission tour until summer 2010. This will give us the chance to uncover even more of the mysterious ring structures and answer some of the questions in queue.

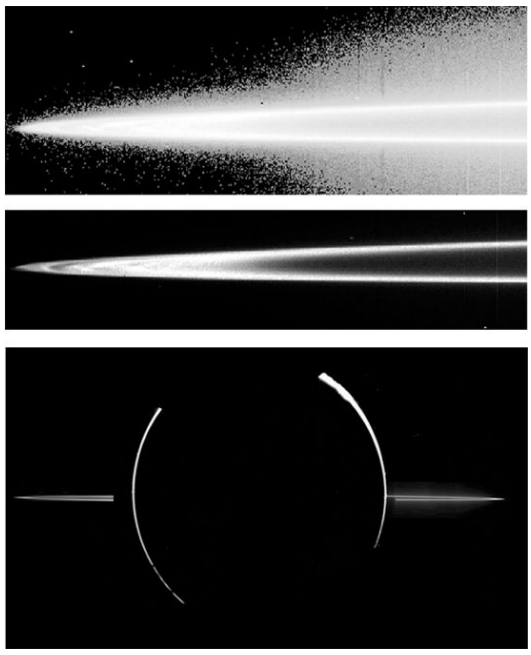

(a) Rings around Jupiter

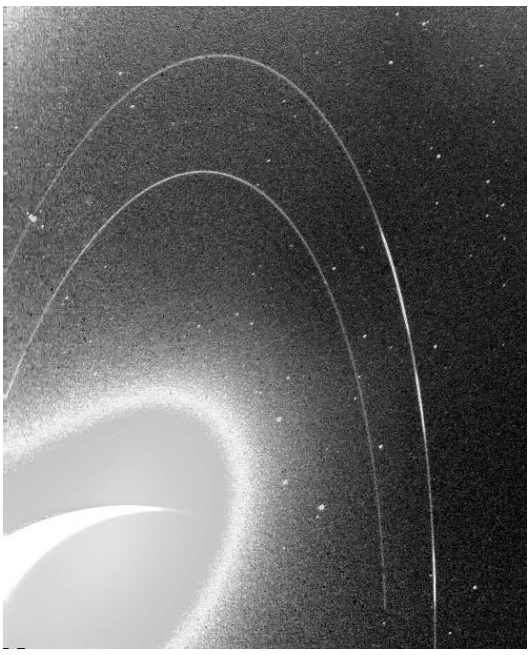

(b) Rings around Neptune

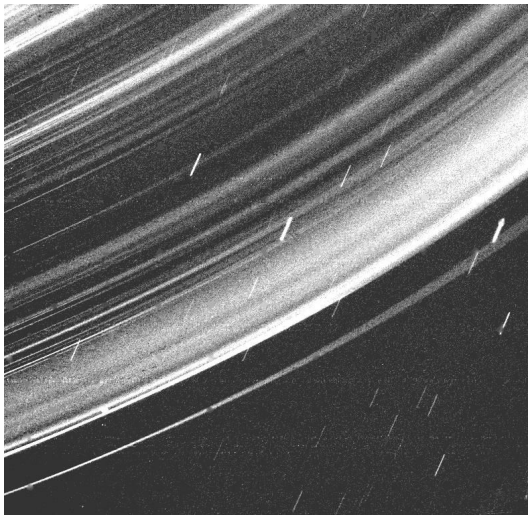

(c) Rings around Uranus

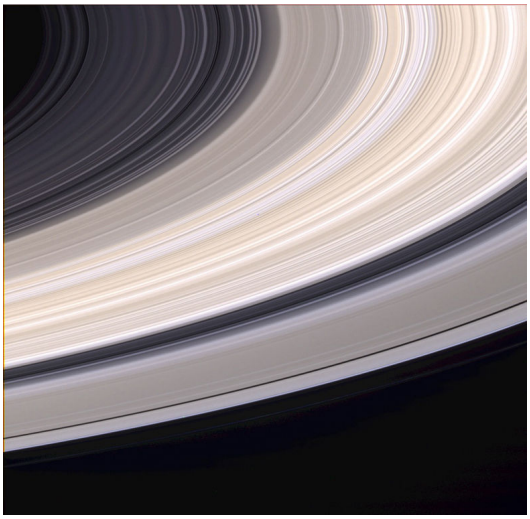

(d) Rings around Saturn

Figure 1.1 The two upper Galileo images (1996) of panel **(a)** show Jupiter's main ring surrounded by an halo (top) and the main ring itself (middle). The bottom image in panel **(a)** depicts Jupiter's main ring as a mosaic of Voyager images (1979), taken from Jupiter's shadow looking towards Sun. Jupiter itself is seen by the lightened atmosphere (circular arcs), the main ring by micron-sized dust scattering light into the camera lens. Jupiter as well as its shadow separate the main ring into two ring arms, seen on the left and right from the planet. Panel **(b)** shows a wide-angle Voyager 2 image (1989) of Neptune's two main rings at 135 ° phase angle (Sec. 3.4.2). A part of the Uranus ring system is shown in panel **(c)**, also taken from Voyager 2, in the shadow of Uranus at a distance of approximately 236000 km from Uranus. A natural color view of Saturn's rings was taken by Cassini in summer 2004, nine days before orbit insertion, panel **(d)**. The B ring is the bright wide part, curving from upper right to lower left in this image. The dark strand, just right to the B ring, is the Cassini division, separating the B and outer A ring. Further out, we find an even smaller dark strand, the Encke gap, which is maintained by *Pan*, a 25 km sized moon. Credit: www.ciclops.org

Planetary rings comprise those charming entourages of all the giant planets in our outer solar system. Jupiter, Neptune, Uranus, and Saturn are blessed by such extremely flat, but wide add-ons (Fig. 1.1). Besides being beautiful to look at, planetary rings exhibit a wealth of observable features, providing hints about physical processes and mechanisms that shape our universe. Almost evolved to thermal equilibrium, ring material has little random motion apart from its circular orbital motion in a plane around the central planet. This is the reason for the enormous dimensional contrast in vertical-to-horizontal extend of planetary rings. The extension of Saturn's rings for instance can be visualized by a sheet of paper being spread across a football field.

As shown by Maxwell (1859), and nowadays confirmed by many observational data, planetary rings are far from being solid objects. They contain a myriad of individual bodies encircling the central planet, mostly composed of water ice with traces of silicates. Their size ranges from dust powder of sub-microns up to boulders of skyscraper-like sizes. Figure 1.2 shows an artist concept of a close-up view of Saturn's ring particles.

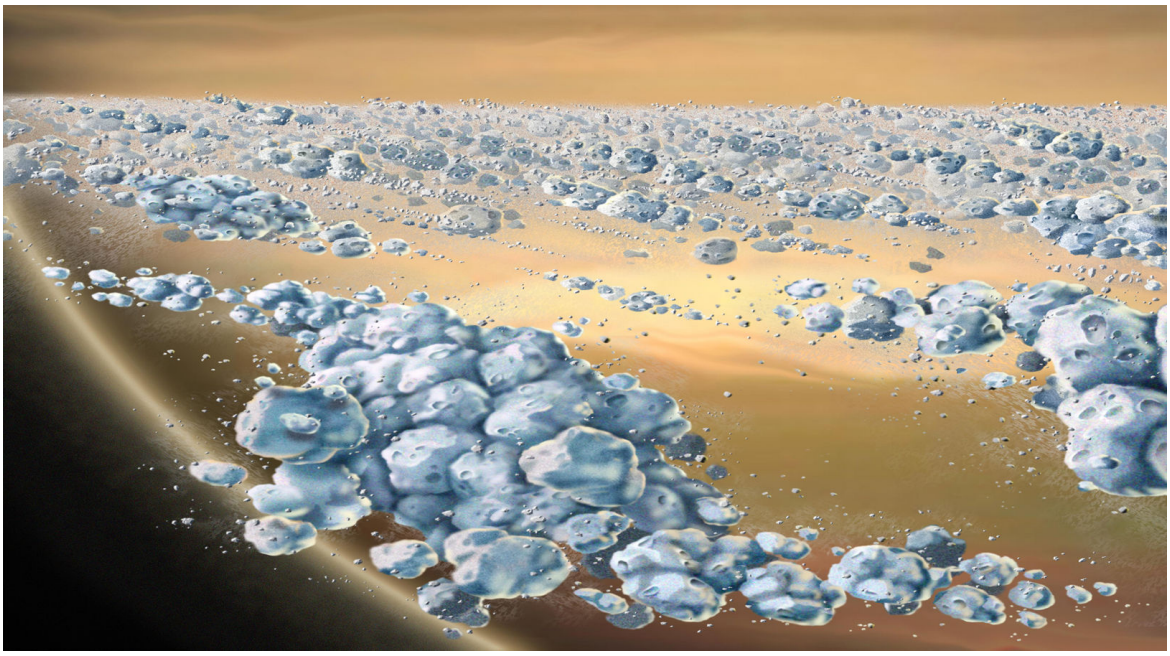

Figure 1.2 Artist concept of a close-up view of Saturn's ring particles. Saturn is visible in the background. The blue particles are composed mostly of ice. Adhesion, gravity and other mechanism make them clump, to continually form elongated curved aggregates. Under the influence of Keplerian shear and perturbing forces, these aggregates disperse. Image by M. Peterson, based on a 1984 image by William K. Hartmann. Credit: www.jpl.nasa.gov

Usually, rings are found in the *Roche zone* of their central planet, the region within tidal forces of the planet's gravity field prevent ring material to coalesce under their own gravity into larger objects. However, we find kilometer large satellites as part of the ring systems, but placed safely outward of the Roche zone. Saturn has more than 60 of them, including *Titan* and *Enceladus*. While the former one has just been found to hold a giant, glassy lake of liquid hydrocarbons (Brown et al., 2008), the latter rather small moon is well known for its cryovolcanic activities and possibly holds an ocean of liquid water beneath its surface (Fig. 1.3).

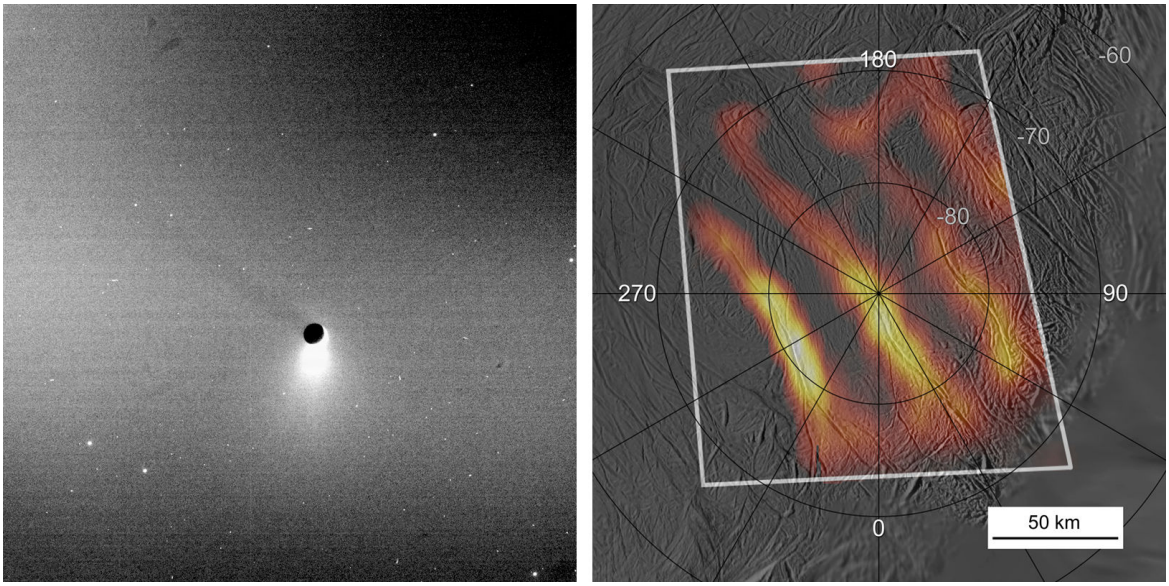

Figure 1.3 Cassini images from the imaging science subsystem (left, 2006), and composite infrared spectrometer (right, 2008). On the left, the icy plume of Enceladus, enlightened by scattered sunlight, while the moon itself casts a shadow onto the the E ring of Saturn. To the right, the south polar region of Enceladus, revealing the warm, 150 km long cracks, which are the vents of the plume material. Credit: www.ciclops.org

Figure 1.4 gives a panoramic overview of the Saturn's ring system. This mosaic is composed out of 165 images taken by Cassini at the end of 2006. As can be seen, the rings are more than one homogeneous appendage of Saturn. Depending on the local material composition, light suffers diffraction, absorption, and scattering to different amounts. The main rings itself are marked by letters, starting at the very faint D ring, followed by the C ring, which inhabits some smaller ringlet structures. The widest and heaviest of all Saturnian rings is the B ring, which in this geometry blocks most of the sunlight. The Cassini division (CD) connects B and A ring, in which the Encke gap (EG) is placed in. At the very edge of the main rings, we see the fascinating F ring. Further out, G and E ring are visible. The latter one being the biggest dust

complex in the solar system is feed by eruptions of the icy plumes on Enceladus, here hardly visible in the E ring's left side edge.

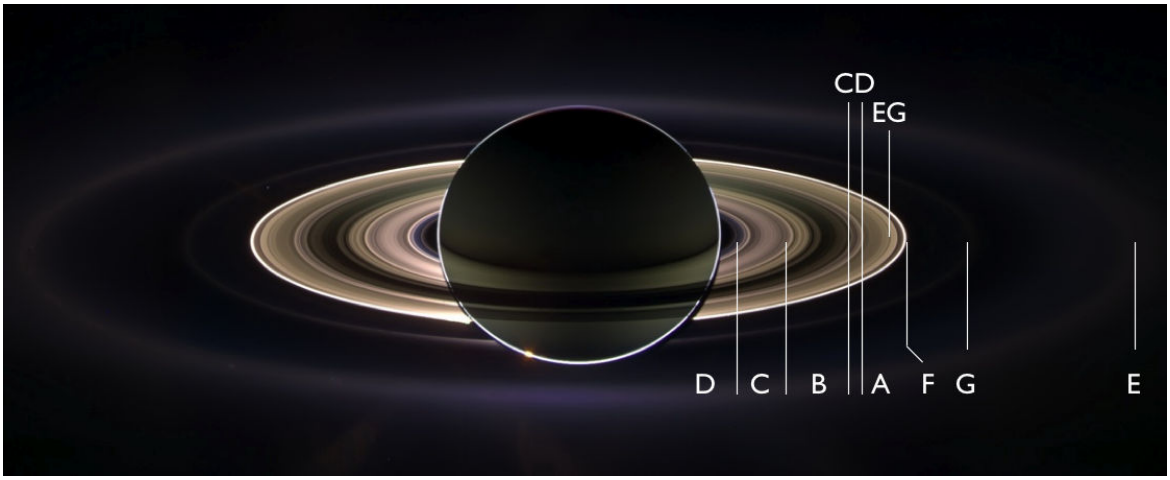

Figure 1.4 This striking panorama of Saturn's rings shows the main rings in its entire extend. The Sun is directly behind Saturn, whereas Cassini was placed in the shadow of Saturn to produce this unique viewing geometry. See text for details. Credit: www.jpl.nasa.gov

The structures being found in the ring system are closely related to the origin of Saturn's rings. Still a riddle to ring scientist, the origin of Saturn's rings seems unique compared to the ones from Jupiter, Neptune, and Uranus. These three system represent very dark material, which has little mass, and may therefore be easily created by disrupted small moonlets. In contrast, Saturn's ring are en gross very brilliant and quite heavy, i.e., roughly the mass of the moon Mimas (400 km across). Consequently, the major part of Saturn's rings seems to be of secondary rather than direct, primordial origin, e.g., dust condensate. Also the mere action of dissipative processes like cosmic erosion, inelastic particle collisions, drag forces (plasma etc.) vote against a primordial origin of the rings. Taking this point of view, there are likely two scenarios in favor of ring formation:

- Rings are remainders of disrupted moons or other fly-by bodies, that could not bear up against tidal forces of Saturn (Dones, 1991).
- Rings are remainders from locally formed moons, that have been destroyed by incoming projectiles (Lissauer et al., 1988).

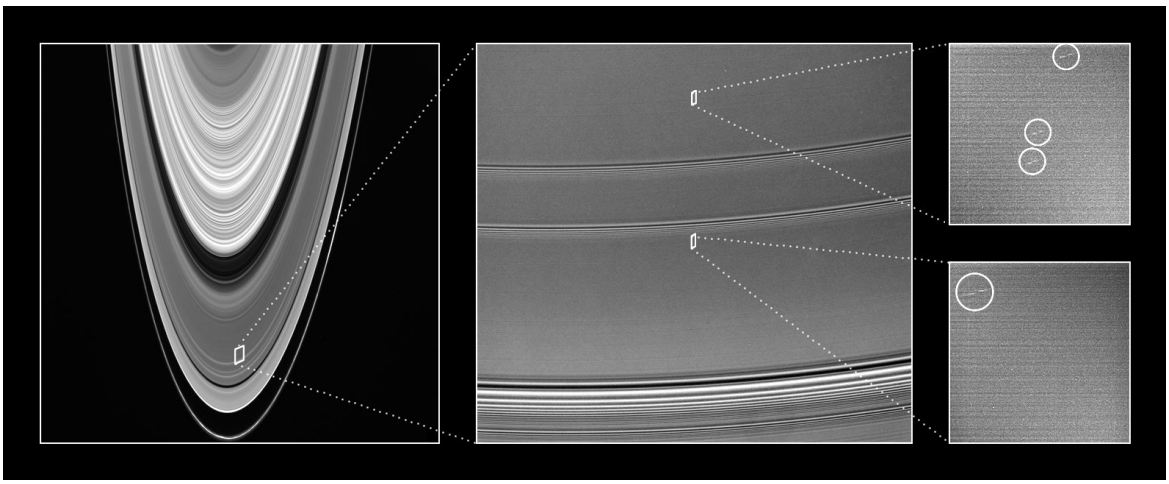

Figure 1.5 Propellers in the A ring. It is believed, that these propeller like structures provide the first direct observations of moonlets approximately 100 m in size. The propellers itself are about 5 km long and remain constant as they orbit Saturn. In the center image (close up of the A ring), a density wave caused by the moons Janus and Epimetheus can be seen at the bottom. Credit: www.jpl.nasa.gov

These two scenarios are also supported by reported moonlets (60 - 140 m across), which are embedded in the main rings. Moonlets of such size produce *propeller*-like structures (Tiscareno et al., 2006, Spahn and Schmidt, 2006, Sremčević et al., 2007), which can be used to identify them (Fig. 1.5). Larger moonlets, are able to evolve these propellers towards gaps. This is observed in the Encke and Keeler gap (Fig. 1.6). Both gaps are the result of gravitational interactions between ring material and the embedded moonlets. The Encke gap is swept-free by Pan, whereas the Keeler gap is carved by Daphnis.

Historically, the Encke gap has been reported by Keeler in 1888 (Keeler, 1889) as a thick black line in the outer A ring. In 1954 however, its existence has been questioned by Kuiper, using the 200 inch Hale reflector. It was until the late 1970's, that the Encke gap has been seen during an eclipse of the moon Iapetus by the rings (Reitsema, 1978) and clearly identified by Pioneer 11 (Gehrels et al., 1980). During a stellar occultation, Ainslie (Ainslie, 1917) has probably been the first to observe what we now call the Keeler gap. Confusingly, the international nomenclature committee named Keeler's discovery after Encke and Ainslie's discovery after Keeler.

In this work, we focus on the central Encke gap ringlet. Beside being knotted and kinky (Fig. 1.6), it belongs to a particular family of *heliotropic ringlets*, including its inner and outer neighbors in the Encke gap, as well as a ringlet in the outer part of the Cassini division. Such heliotropic ringlets have been reported to maintain a peculiar orientation with respect to Sun (Hedman et al., 2007), i.e., their apocenters are shifted

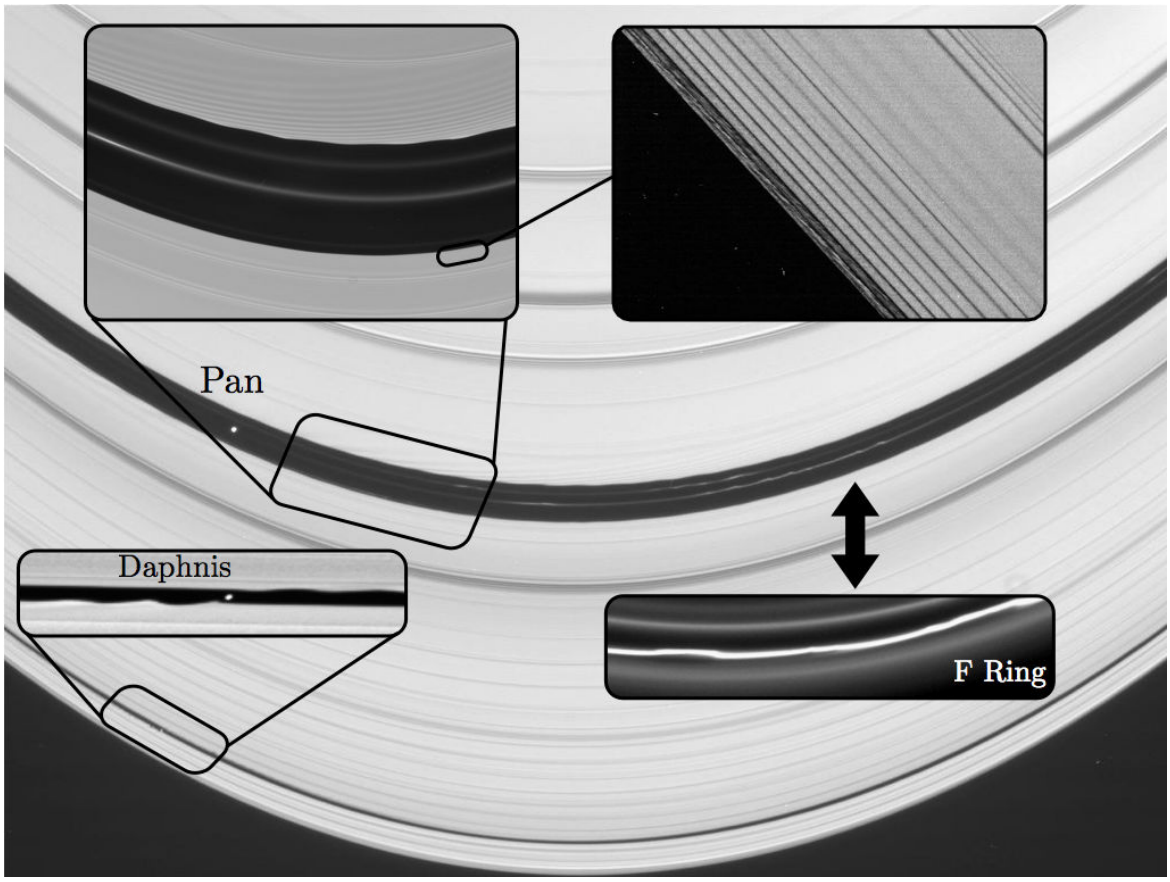

Figure 1.6 This image shows the A ring with its two gaps, Encke and Keeler, including their personal moons, Pan and Daphnis. The close-up view of the Keeler gap reveals the influence of Daphnis onto the gap edges. A wavy pattern -wakes - is induced via gravitational interaction. The same mechanism occurs in the Encke gap, see close-up. The close-up of the outer Encke gap edge reveals regularly spaced dark lanes, 18 ∘ upstream of Pan. This wake structure is induced by Pan. In the Encke gap, there are several ringlets, which have radial and azimuthal brightness variation, which might come from embedded moonlets. Notice, the kinky and knotted structures of the Encke gap ringlets conspicuously resemble structures in the F ring. Credit: www.jpl.nasa.gov

tens of kilometers towards Sun. This is quite remarkable from the dynamical point of view. Dynamically, one would expect eccentric features in the Saturnian rings to precess around Saturn over periods of months at a rate mainly determined by Saturn's oblateness.

A sharp radial confinement of the ringlets can be seen in Fig. 1.6, and has been reported by many authors. For instance, Porco et al. (2005) report drop-offs in the optical depth (Sec. 3.4.2) on the scale of meters from roughly 10^{-2} down to zero. These features point to the action of embedded moonlets even others than Pan in the case of the Encke gap. Such moonlet-family might be the key-ingredient for the

existence of faint ringlets.

This work is organized as follows: In the two subsequent chapters, we investigate the pure kinematics of dust grains and the structure that comes with it. Any kinetic interactions are neglected, presuming a timescale separation of kinematics and kinetics. In chapter 3, we apply our kinematic model to the Encke gap and relate our analytical findings to observations, discussing very briefly some fundamentals of photometry. The kinetic theory is addressed in chapter 4, where we investigate lifetimes and possible mechanism that steadily replenish the ringlet with material. Finally, chapter 5 gives conclusive remarks as well as an outlook to further investigations.

CHAPTER 2

Circumplanetary Dust-Dynamics In The Solar System

According to Kepler's laws, most celestial objects in our solar system move on ellipses in the gravity field of a massive central body. Perturbation forces lead to variations of this Keplerian-like motion, although their relative strengths may vary significantly from one situation to another. Following planetary gravity, the strongest forces acting on circumplanetary micrometer-sized dust grains are: solar tides, solar radiation pressure, planetary oblateness, and Lorentz force. The first one is important for the orbits of grains far from planets, while the latter two dominate in the planet's vicinity. At intermediate distance, all four forces may be simultaneously important, depending on the grain's size.

2.1. Extended Newton Kinematics

In order to get some non-trivial motion of dust grains in orbit about a planet the left-hand side of Newton's second law $\mathbf{F} = m\mathbf{a}$ is extended by additional forces, which brings additional non-linearities in the equations of motion and do often not allow for analytical solutions. Nevertheless, using *osculating orbital elements* in conjunction with perturbation theory it is possible to find the characteristic properties of the studied system.

Figure 2.1 shows one possible set of the six osculating orbital elements $(\Omega, \varpi, i, e, a, T)$, which are equivalent to the canonical description via space-momentum coordinates. The first three variables *longitude of ascending node* (Ω), *longitude of pericenter* (ϖ), and *inclination* (i) describe the orientation of the ellipse with respect to the ecliptic, whereas *eccentricity* (e) and *semi-major axis* a define shape and extend of the ellipse. T corresponds to the time of pericenter passage. Of course, other choices are possible, e.g., Danby (1988). For small perturbations one finds periodic variations of the

Keplerian orbital elements around the *free* ones. *Free* refers to the unperturbed case, where values are solely given by initial conditions and are constants of motion.

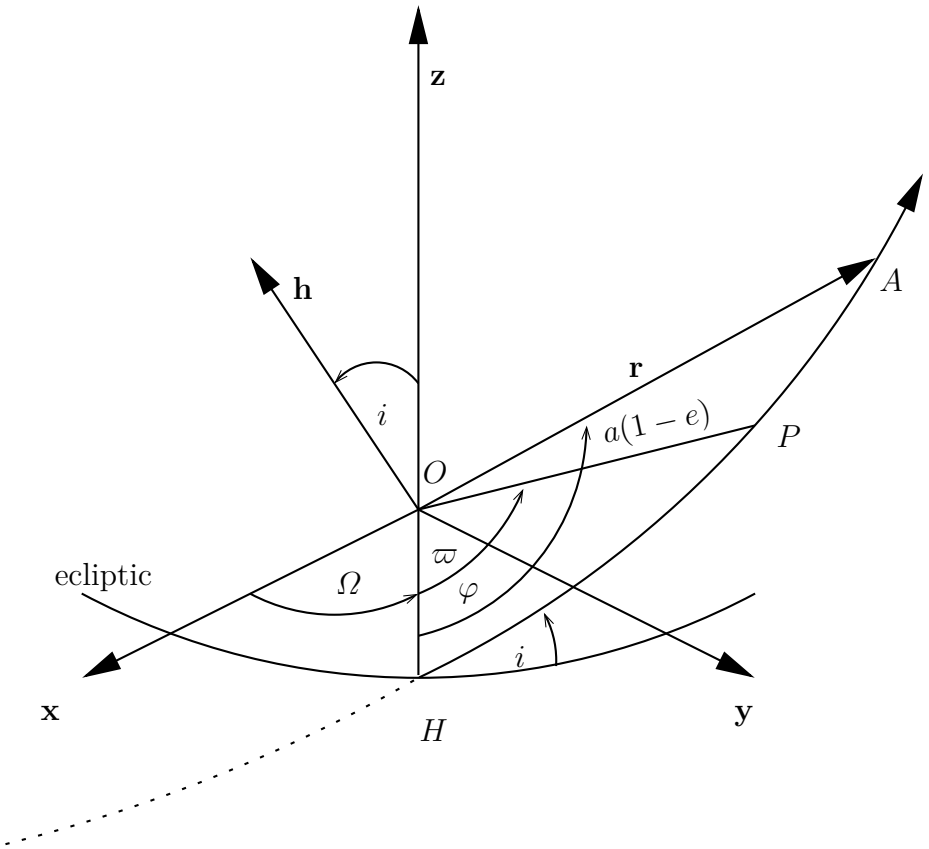

Figure 2.1 One set of possible orbit elements adopted from Danby (1988). The origin O is placed in the center of the planet. Vector **x** points towards the vernal equinox and **z** towards the north pole of the ecliptic. The orbital plane lies in the pie wedge HPO, where the ascending node H marks the point, at which a celestial body rises northward on its orbit. The descending node is on the opposite side, where the body crosses the ecliptic while moving southward. The *longitude of ascending node* is marked by Ω and is measured eastward, as indicated by the arrow. The *inclination* i measures the angle between the plane of the orbit and the ecliptic, or equivalently, between the angular momentum vector **h** and **z** direction. The *longitude of pericenter* is given by ϖ. The remaining orbit elements are given by *semi-major axis* a, *eccentricity* e, and *time of pericenter passage* T. The angle φ measures the local position of the radius vector and is termed *true anomaly*.

2.1.1. Planetary Oblateness

A massive central body is far from being a perfect sphere. This is especially true for non-rigid planets, which are more sensible to mechanical deformation than solid ones. Besides deformation of the planet itself, we also have topographic and - in the case of

Earth - oceanic mass contributions to a nonspherical mass distribution. Thus, particles in orbit of such a dented central body feel a non-uniform gravitational acceleration. The nonspherical mass distribution can be modeled by a multipole expansion of the gravity potential of the central body using Legendre polynomials in a planetocentric spherical coordinate system (r, ϕ, ϑ). Here, r denotes the radial distance from the central planet, ϕ the position of longitude, and ϑ the position of latitude of the particle (Fig. 2.2).

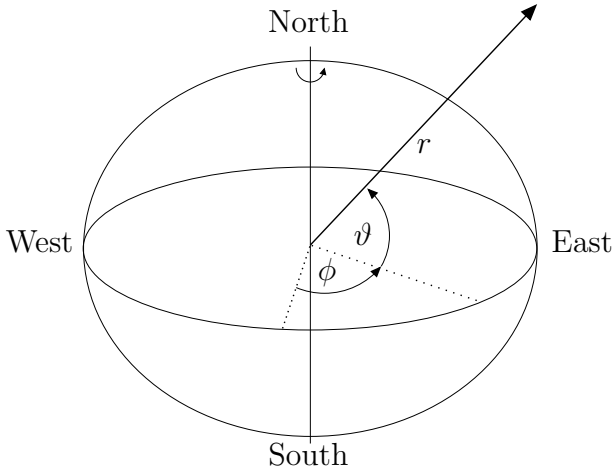

Figure 2.2 Sketch of the inertial frame of reference fixed at the origin of the oblate planet. As illustrated, regions around the north and south pole are flattened due to centrifugal accelerations.

For an ideal spinning planet with a smooth surface, longitudinal variations in the mass distribution may be neglected, making the problem axial symmetric. The assumption of axial symmetry is excellent for planets in our solar system, and the extended gravity potential V to that of a point source in a planetocentric-corotating frame of reference then reads

$$V = -\frac{\mu}{r}\left(1 - \sum_{j=1}^{\infty} J_{2j}\left(\frac{R_p}{r}\right)^{2j} P_{2j}(\sin\vartheta)\right). \tag{2.1}$$

Here, the J_{2j} are dimensionless coefficients, which measure deviations from the spherical mass distribution of a perfect spherical planet (equatorial radius R_p, mass M_p, and $\mu = M_p G$, with gravity constant G). The $P_{2j}(\sin\vartheta)$ are Legendre polynomials of degree $2j$ in $\sin\vartheta$.

Usually we have $J_2 \gg J_{2j}$, $\forall\, j > 1$, i.e., to a reasonable amount of accuracy, gravity potentials of nonspherical planets may be represented by the monopole (Kepler) and quadrupole J_2 term. As a matter of fact, far away from the planet, i.e., several

planetary radii, higher order terms get negligible small, due to the $(R_p/r)^{2j}$ scaling. The lack of the dipole term simply comes from the fact, that the classical mass is always positive. The gravity force $\mathbf{F}_{\mathrm{GR}}$ felt by a particle of mass m is then given by taking the gradient according to

$$\mathbf{F}_{\mathrm{GR}} = -m\nabla V. \tag{2.2}$$

Orbit-averaged equations of motion for this scenario have been first derived by Danby (1988). Solutions are still ellipses, with constant eccentricity and inclination, but harmonic varying positions of pericenter and nodes. To second order in eccentricity and inclination, it can be shown, that the position of pericenter advances, whereas the position of nodes regresses (Danby, 1988).

Remark: Horseshoe- And Tadpole-Like Orbits

Particles that move around planets may also be affected by other gravity sources, including satellites of the planet and dusty rings. This is usually treated as N-body interaction, which in some cases can be dealt with using the restricted circular three body problem or even simple - the Hill's problem. The former one is applicable to problems, where one mass (dust grain) is much smaller than the two others (e.g. Saturn and Pan), the latter problem applies to situations, where the motion in the vicinity of the secondary (e.g. the satellite) is addressed. Hill's problem emerges from the restricted three body problem as an expansion around the position of the secondary, which has to be much less massive than the primary. There have been many studies carried out about this problem. The most relevant work in this context was done by Henon and Petit (1986). They derive parametrized solutions, which can be used to study efficiently the interaction during an encounter of dust grain and moon in the gravity field of a central planet, see also Ida and Nakazawa (1989).

In the Encke gap we have the setup, where the moon Pan shares its orbit with the central ringlet. Certainly, Pan and the ringlet are somehow connected to each other. Pan opens and maintains the gap, while at the same time it forces most of the particles on *horseshoe-* and *tadpole-like* orbits. The names come from the shape of motion in a frame of reference, rotating with the moon (Fig. 2.3).

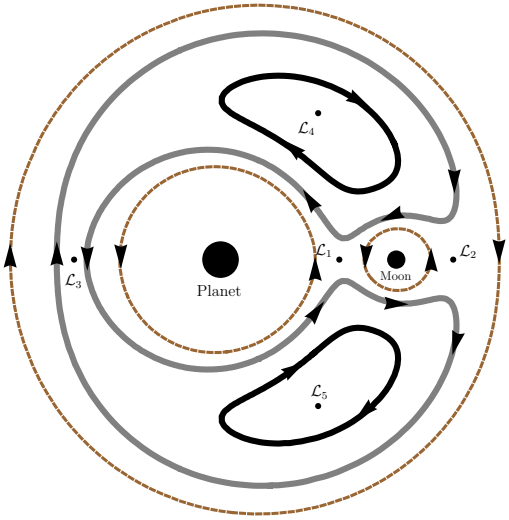

Figure 2.3 Depending on the pseudo-energy (Jacobi-integral), which is the only integral that exists in the restricted three body problem, possible solutions lie outside the regions, encircled by the boundaries of the curves. The two thick black dots indicate the large central planet and the moon, whereas the arrows indicate possible motions of test particles. The frame of reference corotates with the moon. Starting from orbits (brown, dashed) restricted around each individual mass (central planet and moon) or far away around both (outermost, brown, dashed curve), the two innermost circular-like regions as well as the outermost closed curve join to form first horseshoe-like (gray colored region), then tadpole-like (black colored region) motion, when the pseudo-energy is raised. There are 3 joining points, which are referred to as co-linear *Lagrange points*, $\mathcal{L}_{1/2/3}$. At these points, gravitational as well as centrifugal accelerations of central planet and moon balance. Raising the pseudo-energy further on, the restricted horseshoe-like region continuously morphs into the two separated tadpole-shapes, which in the limit of the lowest possible pseudo-energy give the positions of two further Lagrange points, $\mathcal{L}_{4/5}$, of which $\mathcal{L}_4$ is the upper, $\mathcal{L}_5$ the lower one in this image. Notice the flip-flop mechanism, especially for horseshoe- and tadpole-like orbits. This planar view can be extended to three dimensions, where the restricting regions resemble cylinders and spheres.

These shapes - closely related to the zero velocity curves - represent possible exclusion domains of solutions to the restricted circular three body problem, which are in essence quite insensitive to drag forces. This stems from the fact, that the semi-major axes of particles on such special orbits follow a flip-flop mechanism (Dermott et al., 1980, Spahn, 1987).

In detail, at each encounter with the moon (semi-major axis a_0), the semi-major axes of the particles flip from $a_i = a_0 + \Delta a \rightarrow a_f = a_0 - \Delta a$, if the initial semi-major axis a_i lies in the regime of the Hill radius of the moon h_{moon} (Spahn, 1987), which is

given by

$$h_{\text{moon}} \equiv a_0 \sqrt[3]{\frac{M_{\text{moon}}}{3(M_{\text{planet}} + M_{\text{moon}})}}. \tag{2.3}$$

The Hill radius defines the radial extend, to which the gravitational influence of the satellite dominates the one from the central planet. It can also be used, to identify the positions of the 5 *Lagrange points* in the restricted three body problem, at which gravitational as well as centrifugal accelerations of central planet and moon balance.

Since any drag force is related to energy loss, and hence, decrease of semi-major axis, the particles are immune to them on timescales of tens to hundreds of years. The restricted three body problem does not conserve energy, however, in total energy conservation holds so that the entire system losses energy, i.e., the semi-major axis of the moon decreases, but on astronomical timescales.

We note that the flip-flop mechanism requires strict symmetry, which cannot be fully established. For instance, a particle at position of the Lagrange point $\mathcal{L}_1$ feels a slight different force than a particle at Lagrange point $\mathcal{L}_2$ (Fig. 2.3). Positions $\mathcal{L}_1$ and $\mathcal{L}_2$ are only symmetric with respect to the particle's motion, if the moon were infinitely far away from the planet - meeting the conditions for Hill's problem. Additionally, other perturbations may interfere, so that long term dynamics may differ and lose the flip-flop mechanism.

2.1.2. Solar Radiation

Photons of any wavelength carry energy and momentum. Accordingly, when interacting with matter through absorption, emission, or scattering processes, small forces come into play. The net force on a particle exposed to solar radiation including terms of order $|\mathbf{v}|/c$ reads (Burns et al., 1979)

$$\mathbf{F}_{\text{RP}} = \frac{\sigma Q_{pr}}{c} \text{J}_0 \left(\frac{1\text{AU}}{d}\right)^2 \left[\left(1 - \frac{1}{c}\mathbf{v} \cdot \hat{\mathbf{J}}_\mathbf{0}\right) \hat{\mathbf{J}}_\mathbf{0} - \frac{1}{c}\mathbf{v}\right], \tag{2.4}$$

where σ is the cross section of the particle, $\mathbf{v}$ is the particle's velocity in an inertial frame of reference fixed in the center of the Sun. Furthermore, $\hat{\mathbf{J}}_\mathbf{0}$ is the unit vector pointing away from the Sun. The solar radiation energy flux at the distance of Earth ($d = 1$ AU) is given by $\text{J}_0 = 1.36\,\text{kJ m}^{-2}\,\text{sec}^{-1}$. For Saturn we have $d = 9.58$ AU. Finally, Q_{pr} is the dimensionless radiation pressure efficiency factor and c is the speed of light in SI units.

The radiation pressure coefficient Q_{pr} - here averaged over the solar spectrum and phase - corresponds to the fractional amount of absorbed and scattered energy per grain. Absorption as well as scattering characteristics are, of course, given by the grain's size, composition and surface topology. From geometrical optics and scattering theory one has $Q_{pr} \in [0 \dots 2]$. For grain sizes (here and thereafter always referred to radius size) bigger than a few microns, $Q_{pr} \approx 1$, whereas for submicrons, the solar pressure coefficient drops below unity, e.g., a grain of size $s \approx 0.1\mu$m has $Q_{pr} \approx 0.3$ (Burns et al., 1979).

In principle, two possible scenarios of particle motion may occur. At first, particles can move on Keplerian-like orbits around the Sun. Then, since solar gravity has the same - but opposite in sign - scaling in the distance as the solar radiation, a reduced mass of the Sun can be introduced to account for the interplay of attractive solar gravity and repulsive solar radiation pressure. Usually, solar gravity dominates solar radiation pressure. However, if the particles are sufficiently small, solar radiation pressure may exceed solar gravity, putting particles on hyperbolic orbits. These particles are called $\beta-$meteoroids.

A second scenario of particle motion is given by circumplanetary motion, i.e., particles move around a central planet, while being exposed to solar radiation. Here, the motion is perturbed, depending on the season and position around the central planet. A simple mass reduction cannot serve further to quantify the effect.

The solar perturbation can be split into direct radiation pressure - the velocity independent term in Eq. (2.4) - and velocity dependent Poynting-Robertson drag (second and third terms in Eq. (2.4)). The latter results from a net mass loading of the *moving* particle being in thermal equilibrium with the solar radiation field. In particular, re-radiation of the absorbed energy is isotropic in the frame of reference of the particle. Thus, in a helio-/planetocentric frame of reference, the radiated energy has a net momentum component in tangential direction of the orbit. Conservation principle holds, and hence, the gain of momentum by re-radiation must be compensated by an equal amount of momentum loss of the radiating particle. This results in a net mass loading and causes the semi-major axis to decrease; the action of an effective radiative drag.

As discussed by Burns et al. (1979), Poynting-Robertson drag has little effects on orbit-averaged motion and is therefore neglected in the following. In contrast, direct radiation pressure noticeably affects the orbit-averaged motion, and therefore needs to be taken into account. In particular, reasonably far away from the Sun, a particle's orbit around a massive planet is mainly characterized by a rise of eccentricity. In such a

situation, the solar radiation direction and magnitude is assumed to be constant, since the orbital period of the planet is much longer than the one of the particle around the planet. Notice that both, Poynting-Robertson drag as well as direct radiation pressure, are purely non-relativistic effects. A coherent treatment of non-relativistic as well as relativistic effects is given in Burns et al. (1979).

Concerning a periodic forcing due to planetary shadow, Mignard (1984) has shown that these effects are of minor importance, leading to small oscillations in the semi-major axis. There are also charging and sputtering mechanism by solar radiation, which indirectly influence the evolution of the particle's orbit. The former mechanism is discussed in the following subsection, whereas the latter one is addressed in chapter 4.

Shapes of lunar microcraters, and those found on returned spacecraft detectors point towards nearly spherical impact projectiles. Motivated by this observational fact, particle shapes are usually assumed to be spherical. From the theoretical point of view, one can show that mean optical responses of irregular shaped particles may be well represented by spheres. However, irregular particles are more efficient scatterers per unit mass due to their large surface area, and additionally more isotropic, i.e., forward- and backward scattering is less developed. Given an ensemble of irregularly shaped grains, the radiation pressure causes a stochastic diffusion of the orbital elements, as discussed in (Makuch et al., 2006, Spahn et al., 2003). Assuming spherical shapes, orbit-averaged equations of motion for micron-sized particles have comprehensively been derived by Burns et al. (1979) and Chamberlain (1979).

2.1.3. Lorentz Force

Planetary magnetic fields trap electrons and ions to form a plasma. Dust grains, which are being plunged into such a plasma suffer charging effects by a variety of mechanisms. The most dominant ones being sweep-up of electrons and ions, which gyrate around the magnetic field lines. The electron's thermal speeds are usually much higher than those from the ions, and hence, uncharged dust grains are more frequently hit by electrons, charging them more negatively. While the grains become more and more negative, the electron current goes down. At the same time, ions can more easily attach to the negatively charged grains. In the end, a balance between electron and ion flux is attained; typically in a fraction of an orbital period (Hamilton, 1993). The grain charge Q can be related to the surface potential Φ via (Horanyi, 1996)

$$Q \simeq 700\, Q_{\mathrm{e}} \left(\frac{\Phi}{1\mathrm{V}}\right) \left(\frac{s}{1\mu\mathrm{m}}\right) \tag{2.5}$$

with elementary charge

$$Q_{\mathrm{e}} \approx -1{,}6 \cdot 10^{-19}\,\mathrm{C}. \tag{2.6}$$

The charging time of a dust grain is proportional to the inverse of its radius size s. Therefore, larger particles reach their equilibrium potential faster than smaller ones. However, their charge-to-mass ratio Q/m is smaller, so that usually Lorentz acceleration of micron-sized dust grains can be neglected. Note that charging of dust grains is a highly fluctuating process, so that the balance between electron and ion fluxes only holds on average.

There are two additional noteworthy mechanism that make grain charging even more complicated, i.e., secondary electron emissions as well as photoelectron currents. Generally, these two contributions are treated as perturbations to the equilibrium grain charge. A detailed discussion on a number of possible charging mechanisms, including the ones adumbrated in this work, can be found in Goertz (1989).

The Lorentz force $\mathbf{F}_{\Phi}$ of a dust grain is determined by the local magnetic field $\mathbf{B}$ and - assuming an infinite-conductivity magnetosphere that corotates rigidly with the planet at rotation rate Ω - by the corotational electric field

$$\mathbf{E_c} = \sqrt{4\pi\epsilon_0}(\mathbf{r} \times \Omega) \times \mathbf{B}, \tag{2.7}$$

with vacuum permittivity ϵ_0. Thus, in an inertial planetocentric coordinate system, the Lorentz force reads (Hamilton, 1993),

$$\mathbf{F}_{\Phi} = Q\left(\dot{\mathbf{r}} \times \mathbf{B} + \mathbf{E_c}\right). \tag{2.8}$$

The magnetic field $\mathbf{B}$ can be described by a gradient of the magnetic potential $\phi_{j,k}$, which can be expanded in spherical harmonics, e.g., Hamilton (1993). Then, the total magnetic field is given by

$$\mathbf{B} = \sum_{j=1}^{\infty} \sum_{k=0}^{j} \mathbf{B}_{j,k} \tag{2.9}$$

with

$$\mathbf{B}_{j,k} = -\nabla \Phi_{j,k}, \tag{2.10}$$

and the j,k components of the scalar magnetic potential, given by the expansion in spherical harmonics in a frame rotating with the planet,

$$\Phi_{j,k} = R_p \left(\frac{R_p}{r}\right)^{j+1} \left[g_{j,k} \cos\left(k(\phi - \Omega_p t)\right) + h_{j,k} \sin\left(k(\phi - \Omega_p t)\right) P_{j,k}(\cos\vartheta)\right]. \quad (2.11)$$

The expression for the Schmidt-normalized associated Legendre polynomials $P_{j,k}$ in terms of the usual Legendre polynomials can be found in Schaffer and Burns (1992).

Despite the magnetic field, the Lorentz force itself cannot be expressed as a gradient of a potential. This is due to the velocity dependence of the force. Here, the typical disturbing function (=perturbation potential) approach does not work and one has to go back to the Gauss' form of planetary equations (Danby, 1988). From those, Hamilton (1993) derives time-averaged perturbation equations for the orbital elements. Considering the axisymmetric case of an aligned dipole, Hamilton (1993) shows, that electromagnetic forces have nonzero contributions to variations in eccentricity and inclination, although to powers of $\sin i$ and e. Being therefore very small, the major effect for small inclination and eccentricity is that of the solar radiation pressure, i.e., precession of longitude of pericenter and nodes. This could have been expected, since most of the gradient of the electromagnetic as well as radiation force varies - at least near the equatorial plane - in radial distance and direction.

2.2. Expected Magnitudes Of The Perturbing Forces

In order to quantify the perturbing strength of the additional forces, we follow Hamilton and Krivov (1996), and take their dimensionless force parameters, which we evaluate for expected dust grain sizes in Saturn's environment at planetary distance of 2.21 R_{Saturn}, i.e., Encke gap mean center.

2.2.1. Planetary Oblateness

The oblateness parameter $\mathcal{W}$ is defined by

$$\mathcal{W} \equiv \frac{3}{2} J_2 \left(\frac{R_p}{a}\right)^2 \frac{n}{n_\odot} \quad (2.12)$$

with mean motion of the particle around the planet

$$n = \sqrt{\mu / a^3}. \quad (2.13)$$

The planetary orbit is assumed to be circular with mean motion about the Sun $n_\odot = \sqrt{\mu_\odot/d^3}$ (d is the distance from Sun, $\mu_\odot = G \quad M_\odot$, $M_\odot$ mass of the Sun). Note, that the ratio (2.13) puts the perturbation due to oblateness (J_2) into the relation of that of solar tides ($n_\odot$). For Saturn we have $n_\odot \approx 0.21\,\mathrm{year}^{-1}$, and hence $\mathcal{W} \approx 94.75$.

2.2.2. Solar Radiation Pressure

The radiative parameter $\mathcal{C}$ is defined by

$$\mathcal{C} \equiv \frac{3}{2}\frac{n}{n_\odot}\Sigma \tag{2.14}$$

with the ratio Σ of radiative force to Saturn's point source gravity force for a circular orbit at planetary distance a,

$$\Sigma = \frac{F_{\mathrm{RP}}}{F_{\mathrm{GR}}} = \frac{3J_0 Q_{pr} a^2}{4\rho c d^2 s}. \tag{2.15}$$

Again, the solar tides are also taken into account. Assuming a radiation pressure efficiency factor of $Q_{pr} = 1$ we find

$$\mathcal{C} \approx 0.49\left(\frac{1\mu\mathrm{m}}{s}\right). \tag{2.16}$$

2.2.3. Lorentz Lorce

The Lorentz parameter $\mathcal{L}$ is introduced by

$$\mathcal{L} \equiv 2\frac{1}{n_\odot}\frac{n^2}{\Omega_p}L, \tag{2.17}$$

where $|L| = \frac{|F_\Phi|}{F_{\mathrm{GR}}}$ measures the ratio of Lorentz force to Saturn's point source gravity force and is given by

$$L \equiv \frac{QB_0R_p^3\Omega_p}{\mu m}, \tag{2.18}$$

whereas solar tides are also considered. Here, B_0 is the magnetic strength at the planetary equator of Saturn, Q and m are the grain's charge and mass, respectively, and Ω_p is the angular velocity of the planet's rotation. With $B_0 \approx -21\,\mu\mathrm{T}$, $\Omega_p \approx \quad 14.36\,\mathrm{day}^{-1}$

and $\rho = 1\text{g cm}^{-3}$, the Lorentz parameter evaluates to

$$\mathcal{L} \approx 14.95 \left(\frac{\Phi}{1V}\right) \left(\frac{1\mu\text{m}}{s}\right)^2 . \tag{2.19}$$

In Fig. 2.4 the three parameters are shown as a function of grain size radius. Grains with radius in the micron range are predominately perturbed by planetary oblateness, since radiative and Lorentz parameter drop off quickly. In the submicron range, the Lorentz force dominates.

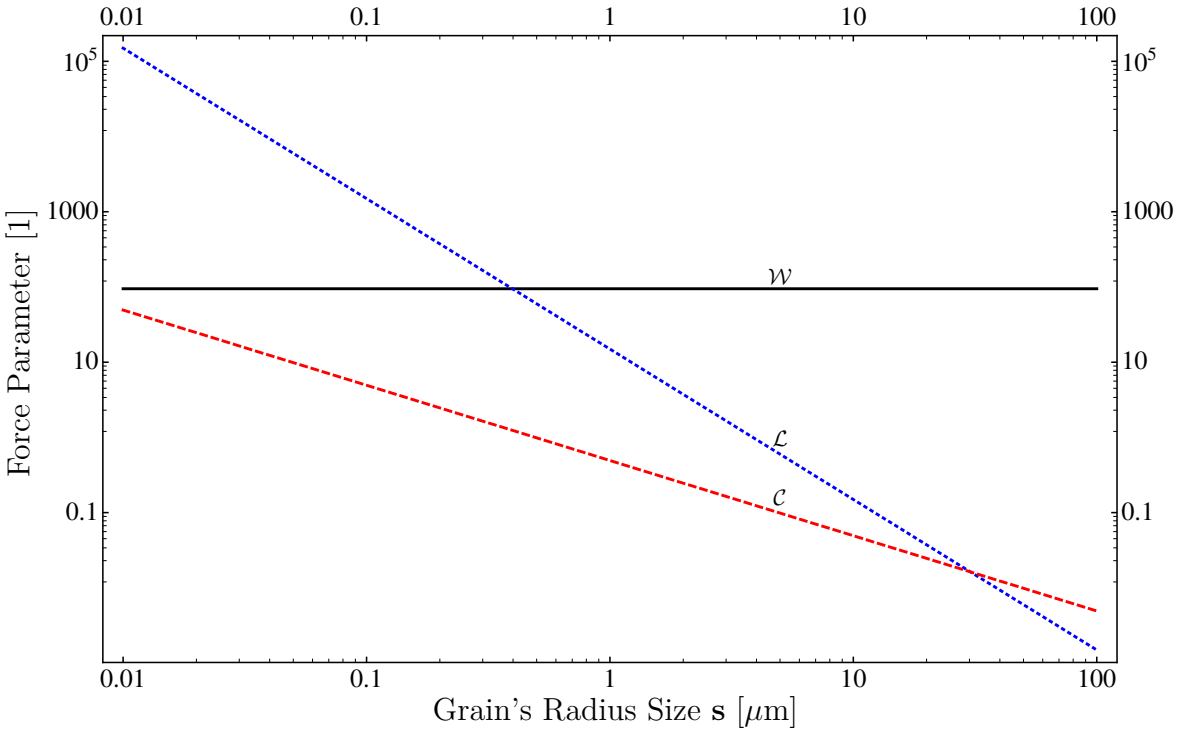

Figure 2.4 Dimensionless force parameters $\mathcal{W}$ (planetary oblateness), $\mathcal{C}$ (solar radiation pressure), and $\mathcal{L}$ (Lorentz force) as a function of grain size evaluated at planetary distance 2.21 R_{Saturn} (mean center of the Encke gap), assuming uniform density $\rho = 1\text{g cm}^{-3}$ as well as a spherical shape of the (icy) grains and surface potential of $\Phi = 1\text{V}$. Roughly, for grains with radius above 1 micron, radiation pressure and Lorentz force drop off quickly making planetary oblateness the most strongest perturbation. In the submicron range, the Lorentz force dominates.

In the context of faint heliotropic ringlets of Saturn, one has to deal with particles in the range of $1 - 100$ microns, so that one may expect Saturn's oblateness to be the most dominant perturbation with respect to the position of the pericenter, while the

Lorentz force contribution is negligible small. Although solar radiation pressure is of the same order as the Lorentz force - at least in the considered size range - it has to be taken into account, since it affects the eccentricity and does not compete with Saturn's oblateness.

CHAPTER 3

The Annulus Model Of Heliotropic Ringlets

Suggested by direct observations (Showalter et al., 1992), the central ringlet of the Encke gap is mostly made up by micron sized, icy particles. These tiny particles are distributed in size and space according to their creation and removal processes in conjunction with dynamical effects, arising from a suite of forces that act on them. The major particle source is most likely to be given by micrometeoroid bombardment of embedded moonlets in the ringlet. This has been suggested by many authors including (Cuzzi et al., 1984, Ferrari and Brahic, 1997, Divine, 1993, Spahn et al., 1999).

The peculiar orientation - *heliotropicity* - of Encke-like ringlets can be astonishingly well explained by three perturbation forces, i.e., planetary oblateness, Lorentz force, and solar radiation pressure. The two former once give rise to precession of an elliptic orbit, whilst the latter increases the orbital eccentricity. Combining both effects yields, in the end, an eccentric ringlet, with apocenter at local noon, pericenter at local midnight, respectively, which indeed corresponds to observational findings.

3.1. The Equation Of Motion

In an inertial frame of reference, the motion of a charged grain (mass m, radius s and charge Q) around an oblate planet exposed to solar radiation can be approximated by (see for instance, Spahn et al., 1999)

$$\ddot{\mathbf{r}} = -\frac{\mu}{r^3}\mathbf{r} - \nabla V_{J_2} + \frac{Q}{m}\left(\dot{\mathbf{r}} \times \mathbf{B} + \mathbf{E_c}\right) + \frac{3\mathbf{J_0}Q_{pr}}{4\rho c d^2 s}, \tag{3.1}$$

with first non-vanishing correction to the gravity field of a point source

$$V_{J_2} = J_2 \frac{\mu}{r} \left(\frac{R_p}{r} \right)^2 \left(3 \sin^2 \vartheta - 1 \right) / 2, \tag{3.2}$$

presuming axial symmetry. The first term on the right-hand-side (forces per unit mass) in Eq. (3.1), $\mathbf{f}_{\text{Kepler}} = -\frac{\mu}{r^3}\mathbf{r}$, corresponds to the case of Keplerian motion in a point source potential. Then, we have the following additional forces per unit mass from left to right in this order, quadrupole moment $\mathbf{f}_{J_2}$ of the gravity potential, Lorentz force $\mathbf{f}_{\Phi}$, and solar radiation pressure $\mathbf{f}_{\text{RP}}$. For details about the forces and nomenclature see chapter 2.

3.1.1. Simplifications

For the purpose of a keen understanding, we restrict ourselves to planar motion. In particular, we consider the particle's orbital plane, the planet's orbital, and the planet's equatorial plane to coincide. This is a good approximation for planets with reasonable low obliquities. Furthermore, we neglect the planet's motion about the Sun, since the expected timescales of the perturbations are of the order of months. For the same reason, we also neglect dragforces, including Poynting Robertson and plasma drag. In fact, particles on the central ringlet in the Encke gap are believed to mainly live on horseshoe- and tadpole-like orbits, which can be regarded as being immune to any dissipative forces on the timescales of months (Ch. 2). Particles on such stabilized orbits are mostly lost during long-term dynamics, or by non-dynamical mechanism, e.g., sputtering or sublimation (Ch. 4).

Close to the planet, the dominant perturbation in the multipole expansion of the gravity potential is given by the quadrupole term J_2. Any other gravitational influences, whether coming from the non-spherical gravity potential of the planet, or possible accompanying dust rings and satellites, or the Sun are neglected. The magnetic field $\mathbf{B}$ is assumed to be of a simple dipole form,

$$\mathbf{B} = \frac{\mathbf{B}_0}{r^3} - 3\frac{\mathbf{r}\,(\mathbf{B}_0 \cdot \mathbf{r})}{r^5} \tag{3.3}$$

$$= \frac{B_0}{r^3} \left(\mathbf{e}_z - 3\,\mathbf{e}_r (\mathbf{e}_z \cdot \mathbf{e}_r) \right), \tag{3.4}$$

located at the planet's center having its dipole moment aligned with the rotation axis of the planet. In the equatorial plane it reads $B = B_0 \left(R_p/r\right)^3$, with the magnetic field strength B_0 at the planet's surface. The charge of the particle is assumed to

be constant. This assumptions is excellent, since most of the stable particles in the Encke-Gap have sizes $s > 1\,\mu$m, which in turn reduces electromagnetic perturbations to a tiny, negligible amount. On the timescale of perturbation, the grain's equilibrium potential of this size class we are dealing with is built up fast (shorter than orbital time scales). This further means, that possible dis- or recharging during planetary shadow passage - for instance due to variation in photo-electron emission or plasma environment - has little effect on the orbital motion. Hence, planetary shadowing is also neglected, which might slightly overestimate the maximal eccentricity, gained via solar radiation pressure.

3.1.2. The Perturbation Equations

Planar Keplerian motion is determined by four free orbital elements, i.e., semi-major axis a, eccentricity e, longitude of pericenter ϖ and mean anomaly. Without any drag forces, the semi-major axis stays constant. Since orbit-averaged equations are being used, perturbations of the mean anomaly, which describes how fast a dust grain circles the planet, are not of interest in our current effort. Thus, only the eccentricity and longitude of pericenter remain to be considered. The forces per unit mass $\mathbf{f}_{J_2}, \mathbf{f}_{\Phi}$, and,

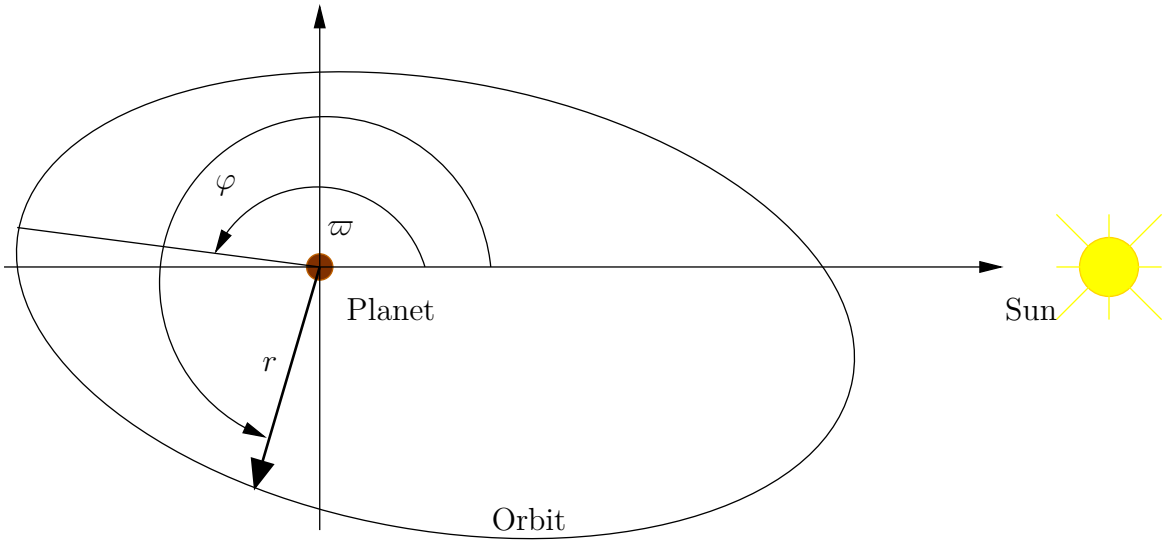

Figure 3.1 Planar geometry of the problem. All angles are measured with respect to the line of sight from planet to Sun. The radial distance from the planet is written as r.

$\mathbf{f}_{\mathrm{RP}}$ can be treated as small perturbations to the Keplerian motion, as long as $|\mathbf{f}_{\mathrm{Kepler}}| \gg |\mathbf{f}_i|$; $i = \{J_2, \Phi, \mathrm{RP}\}$. Following Horanyi et al. (1992), we assume small eccentricities ($e \ll 1$) and use the perturbation equations (Burns et al., 1979, Chamberlain, 1979) in a planetocentric frame of references (Fig. 3.1). The time histories of the three

forced elements a, e, ϖ averaged over one particle orbit (assumed to be constant), as indicated by $\langle\,\rangle$, then read (Horanyi et al., 1992)

$$\langle \dot{a} \rangle = 0 \tag{3.5}$$

$$\langle \dot{e} \rangle = \beta \sin \varpi \tag{3.6}$$

$$\langle \dot{\varpi} \rangle = \frac{\beta}{e} \cos \varpi + \gamma, \tag{3.7}$$

using solar radiation pressure quantity

$$\beta \equiv \frac{3}{2} h f / \mu, \tag{3.8}$$

with specific angular momentum (angular momentum per unit mass)

$$h = \sqrt{\mu a (1 - e^2)} \tag{3.9}$$

and acceleration due to solar radiation pressure

$$f = \frac{3 J_0 Q_{pr}}{4 \rho c d^2 s}. \tag{3.10}$$

Equation (3.7) incorporates the uniform precession rate γ, at which planetary oblateness in conjunction with Lorentz force would move the longitude of pericenter in the absence of radiation pressure (Sec. 2.1.1 - 2.1.3), i.e.,

$$\gamma \equiv \dot{\varpi}_{J_2} + \dot{\varpi}_{\Phi}. \tag{3.11}$$

The precession rate of planetary oblateness is given by (Danby, 1988)

$$\dot{\varpi}_{J_2} = \frac{3}{2} \omega_K J_2 \left(\frac{R_S}{a} \right)^2 \simeq 0.897 \left(\frac{R_S}{a} \right)^{3.5} \text{rad day}^{-1}, \tag{3.12}$$

with Keplerian angular velocity $\omega_K^2 \equiv \mu a^{-3}$. The right-hand-side term gives values of $\dot{\varpi}_{J_2}$ for orbits around Saturn. The precession rate of pericenter provided by the Lorentz force reads (Horanyi and Burns, 1991)

$$\dot{\varpi}_{\Phi} = -2 \frac{\mathrm{Q} B_0}{m} \left(\frac{R_S}{a} \right)^3 \simeq 0.089 \left(\frac{R_S}{a} \right)^3 \left(\frac{1 \mu\text{m}}{s} \right)^2 \left(\frac{\Phi}{1\text{V}} \right) \text{rad day}^{-1}, \tag{3.13}$$

where the right-hand-side term is again evaluated for orbits around Saturn, expressing Q according to Eq. (2.5) in terms of the surface potential, and magnetic field strength at Saturn's surface $B_0 = -21\,\mu$T. Notice that B_0, evaluated at Saturn's equator, is negative owing to its antispin orientation with respect to the corotational magnetic field. The grain mass m is translated into grain size s, assuming uniform density $\rho = 1\,\mathrm{g\ cm^{-3}}$ as well as a spherical shape of the icy grain.

Now there are 3 principle scenarios that might occur to a grain placed into an orbit of a planet under common influences of planetary oblateness, Lorentz force and solar radiation pressure. With respect to the uncharged case, the longitude of pericenter's motion can be

(a) slowed down, with remaining $\gamma > 0$,

(b) stopped, $\gamma = 0$, or

(c) reversed, $\gamma < 0$.

Which of these 3 principle scenarios occurs, depends solely on the grain's size, charge and position in the planet's magnetosphere. For a nominal grain of size 1 micron, placed into the center of the Encke gap, scenario (b) can be established with a grain potential of $\Phi \approx -7$ V. As a matter of fact, surface potentials are rather unknown, however believed to be positive, small of the order of Volts. A comparison of Eqs. (3.12) and (3.13) shows the dominant contribution of planetary oblateness for particles in the micron range, even for surface potentials of the orders of volts. This is due to the grain size scaling of the Lorentz force, which is $\propto s^{-2}$ (see also Sec. 2.2). Consequently, Lorentz force contribution may be safely neglected for particles bigger than a few microns, which in turn makes the precession rate γ independent of the grain size.

3.2. Solutions

3.2.1. Solution For Arbitrary Initial Conditions

Horanyi et al. (1992) derived solutions for vanishing free eccentricity for the model given by Eqs. (3.6), (3.7) to describe the dynamics of the forced eccentricity. Here, we follow their approach to find solutions for non-vanishing free eccentricity by trans-

forming to the variables

$$q \equiv e\cos\varpi \tag{3.14}$$

$$p \equiv e\sin\varpi, \tag{3.15}$$

omitting the indication for the orbit average $\langle\cdot\rangle$ here and in the following. In this new set of variables, it is straight-forward to cast Eqs. (3.6), (3.7) into the form

$$\ddot{q} + \gamma^2(\beta/\gamma + q) = 0, \tag{3.16}$$

which is known to be the equation of motion for an undamped pendulum. The general solution reads

$$q(t) = A\sin(\pm\gamma t + \alpha) - \beta/\gamma, \tag{3.17}$$

with amplitude A and phase α, determined by the initial (=free) conditions, Eq. (3.20), (3.21) below. The $\pm$ sign accounts for the choice of time-direction. Without any loss of generality, we choose $t \in \mathbb{R}_+$, and accordingly drop the negative sign. Transforming back to the initial variables e and ϖ, the solutions take the form of two coupled transcendent equations

$$\varepsilon^2 = \kappa^2 + 1 - 2\kappa\sin(\gamma t + \alpha) \tag{3.18}$$

$$\sin\varpi = -\frac{\kappa}{\varepsilon}\cos(\gamma t + \alpha), \tag{3.19}$$

with $\varepsilon \equiv e\gamma/\beta$ and $\kappa \equiv A\gamma/\beta$. Inserting initial conditions (e_0,ϖ_0) into equations (3.18) and (3.19) determines amplitude and phase via

$$\kappa = \sqrt{\varepsilon_0^2 + 1 \pm 2\varepsilon_0\cos\varpi_0} \tag{3.20}$$

$$\cos\alpha = -\varepsilon_0\sin(\varpi_0)/\kappa. \tag{3.21}$$

3.2.2. Solution For Simplified Initial Conditions

Consider the case of an initial circular orbit, which corresponds to the limit of zero initial eccentricity, i.e., $\varepsilon_0 \to 0$. Then, from equation (3.20), we have $\kappa \to 1$ and from (3.21) $\alpha(\mathrm{mod}\,\pi) \to \pi/2$. Note that both, amplitude κ and phase α, are determined by the initial eccentricity $\varepsilon_0 = 0$. At first sight, the initial longitude of pericenter ϖ_0 may take any value between 0 and 2π, which accounts for its degenerated state on circular orbits. From physics however, circular orbits gain eccentricity due to solar radiation

pressure (Sec. 2.1.2), which, on orbital timescales, has a unique flux direction, and hence, determines the initial longitude of pericenter.

In our planetocentric frame of reference the orbit-averaged longitude of pericenter is *always* born at $\varpi_0 = \pi/2$ for $\varepsilon_0 = 0$. This is of crucial importance for the heliotropic structure, since a coherent phase relation between all longitudes of pericenter and eccentricities is maintained. Finally, from Eq. (3.18) and (3.19) we find the solutions given by Horanyi et al. (1992) for zero initial eccentricity,

$$e(s,t) = \frac{2\beta(s)}{\gamma} \left| \sin\left(\frac{\gamma}{2}t\right) \right| \tag{3.22}$$

and

$$\varpi(s,t) = \left(\frac{\gamma}{2}t \bmod \pi\right) + \frac{\pi}{2}. \tag{3.23}$$

Of course, both elements also vary with surface potential Φ and semi-major axis a through the precession rate γ, which is also a function of grain size. We do not explicitly mark these dependencies in the equations for the precession rate, since once again, its variation with surface potential and grain size is rather weak for micron sized particles immersed in an electromagnetic potential of the order of several volts (Eq. (3.12), (3.13)). The dominant effect is caused by planetary oblateness, which solely depends on the semi-major axis (Sec. 2.2). At the Encke gap, precession rate γ is essentially independent of grain size and surface potential, which we assume in the following by setting $\varpi_\Phi \equiv 0$. It should be noted here, that one may expect other reduced plasma components due to the presence of the rings, so that charging is mainly caused by UV radiation giving positive charge. Latter just enhances the precession induced by J_2, which means, that $\varpi_\Phi = 0$ does not change the picture.

Using (3.22) we define the maximum eccentricity as the ratio

$$e_{\max}(s) \equiv \frac{2\beta(s)}{\gamma}, \tag{3.24}$$

with $\beta(s) \propto 1/s$. Assuming γ to be fixed, particle size itself influences the maximal eccentricity through solar radiation pressure, i.e., smaller particles have larger eccentricity and in turn larger radial excursion during their orbit. Furthermore, a particle of given size s (fixed $\beta(s)$) may have any eccentricity between 0 and 1, as long as the planetary environment allows for the demanded precession rate γ. Usually, this is not the case, which in turn puts constraints on expected particle size distributions for a

given planetary setup. In most cases, the radial excursion can be limited by either gap edges (in case of the Encke gap), central planet or other celestial objects the particles might impact on. This constraints the maximal possible eccentricity via

$$e_{max}(s) \leq e_c, \tag{3.25}$$

e_c being the critical eccentricity derived from the maximal possible radial excursion, which immediately results in a lower size limit $s_{\min}$. If such a critical eccentricity exists, we can parametrize the maximum eccentricity as

$$e_{max}(s) = e_c \frac{s_{\min}}{s}. \tag{3.26}$$

For the Encke gap, particles in the range $1 - 100$ microns are expected (Hedman et al., 2007). From Eq. (3.26) however, the minimal "allowed" grain size evaluates to $s_{\min} = 8.7\,\mu$m, assuming circular gap edges and a gap width of $p = 320\,$km, which translates into a critical eccentricity of $e_c \approx 1.2 \cdot 10^{-3}$. Particle with $s < s_{\min}$ are removed by the gap edges, since their radial excursion due to the increased orbital eccentricity by radiation pressure exceeds e_c.

It is instructive to have a look at the timescales, on which the eccentricity and the longitude of pericenter vary. They are roughly given by

$$t_e \propto \frac{e}{\dot{e}} \approx 2/\gamma \quad \text{and} \quad t_\varpi \propto \frac{\varpi}{\dot{\varpi}} \approx 2/\gamma. \tag{3.27}$$

For microns sized particles in the Encke gap, we have (Lorentz force neglected) $t_e = t_\varpi \approx 112$ days, independently of the particle size. Half of this timescale corresponds to maximal eccentricity and passage of the pericenter through the midnight position with respect to Saturn.

To put it more generally, ringlets that show the heliotropic property are formed by material with lifetimes greater or at least equal to about

$$t_{\text{life}}^{\text{low}} \approx 2/\gamma. \tag{3.28}$$

Note that this holds for arbitrarily uniform precession rate γ, including the Lorentz force. This lower lifetime limit can be used to constrain the maximal strength of the sink, at least for heliotropic ringlets, discussed in chapter 4.

3.3. Annulus Generation

3.3.1. From Orbital Elements To Streamlines

Solutions (3.22) and (3.23) can be translated into streamlines, which represent solutions to our problem in the spatial phase space. In polar-coordinates, a streamline is defined by radial component r and longitude φ (Fig. 3.1). The radial component at longitude φ with given position of pericenter ϖ, eccentricity e and semi-major axis a of a particle with radius size s is given by

$$r(\varphi,\varpi,s) = \frac{a(1-e(\varpi,s)^2)}{1+e(\varpi,s)\cos(\varphi-\varpi)}, \tag{3.29}$$

with eccentricity re-expressed from equations (3.22), (3.23) and (3.24) as

$$e(\varpi,s) \equiv e_{\max}(s)\sin(\varpi-\pi/2). \tag{3.30}$$

Let's have a look at the equations (3.22)-(3.23) and (3.29)-(3.30), and trace a cycle of eccentricity build-up as shown in panel **(a)** of Fig. 3.2. The lower panel **(b)** depicts several orbits (black) for the nominal grain at different phases of the precession cycle. The Sun is located on the right side of the page, i.e., the solar flux travels from right to left. For clarity, eccentricity has been scaled by a factor 10^3 in panel **(b)**. The orange, numbered points correspond to the subsequent time steps of panel **(a)** and indicate the actual longitude of pericenter.

Assume a nominal grain of given radius size $s = 33\mu$m is born on a circular orbit (= zero initial eccentricity) about Saturn at arbitrary azimuthal position ϖ having semi-major axis $a = 2.21\,R_{\rm Saturn}$ and zero inclination. Solar radiation pressure starts to increase the eccentricity of the particle, i.e., the particle is accelerated on the local noon-midnight side of its orbit (lateral east-side of Saturn with respect to Sun) - birth of pericenter at $\varpi = \pi/2$ - and decelerated on local midnight-noon side - birth of apocenter at $\varpi = 3\pi/2$. Note, both longitudes are orbit-averaged, i.e., the maximal acceleration can be found at these two positions.

Under the influence of Saturn's oblateness, and possibly Lorentz force, the longitude of pericenter starts to move in prograde direction. Note, retrograde direction is only possible, if Lorentz force exceeds the force due to planetary oblateness and acts in opposite direction, which is not the case for the Encke gap, i.e., the plasma environment as well as the examined family of grain sizes do not allow for the retrograde case. From symmetry in the dynamics, the maximal eccentricity of the precessing orbit lies

at $\varpi = \pi$ (planetary shadow neglected). After the longitude of pericenter has passed midnight position, the eccentricity starts to shrink until $\varpi = 3\pi/2$. Then, the cycle restarts at $\varpi = \pi/2$. Obviously, the faster the argument of pericenter moves, i.e., larger γ, the smaller is the maximal eccentricity and vice versa (see also Eq. (3.24)).

Having a myriad of nominal grains on different phases of the precession cycle results in an annulus, which is shifted towards Sun. The annulus itself can be described by two enclosing ellipses (inner: green, dashed; outer: blue, dashed), which are functions of the grain size through the maximal eccentricity. Apparently, their *apocenters point towards the Sun*, so that the apocenter of the eccentric annulus, which can be defined by the apocenters of the enclosing ellipses, also points towards Sun. Notice, this orientation of the enclosing ellipses - or equivalently the annulus - must hold for any ensemble of a certain grain sizes that follows such a dynamic, i.e., uniform precession of the pericenter in conjunction with periodic variation of eccentricity.

Semi-major axes and eccentricities for inner (i) and outer (o) ellipses are given by

$$e_i = \frac{e_{\max}(s)}{e_{\max}(s) - 2}; \quad a_i = a\frac{2 - e_{\max}(s)}{2}; \quad \varpi_i = 0, \tag{3.31}$$

and

$$e_o = \frac{e_{\max}(s)}{e_{\max}(s) + 2}; \quad a_o = a\frac{2 + e_{\max}(s)}{2}; \quad \varpi_o = 0, \tag{3.32}$$

whereas the annulus area $\mathcal{A}$ is given by

$$\begin{aligned}\mathcal{A} &= \frac{1}{2}\pi a^2 \left((2 + e_{\max}(s))\sqrt{1 + e_{\max}(s)} - (2 - e_{\max}(s))\sqrt{1 - e_{\max}(s)} \right) \\ &= 2\pi a^2 \left(e_{\max}(s) + \frac{e_{\max}^5(s)}{128} + \mathcal{O}(e_{\max}^7(s)) \right).\end{aligned} \tag{3.33}$$

Clearly, the smaller the particles, the larger the maximal eccentricity, which results in a larger annulus area. This behavior is found in equation (3.33). There exist more than one particular grain size ensemble, so we may expect a continuous overlay of annuli, different in area and particle density, depending on the particle size distribution. From their origin by impact-ejecta process (Spahn et al., 2006), smaller particles are naturally more abundant than larger ones. On the other hand, they have smaller cross-sections, their annuli are very wide and have smaller particle densities. These interplays between particle density, annuls area, and particles' cross sections shape the ringlet profile, including its width, which is indeed found in the Cassini observations.

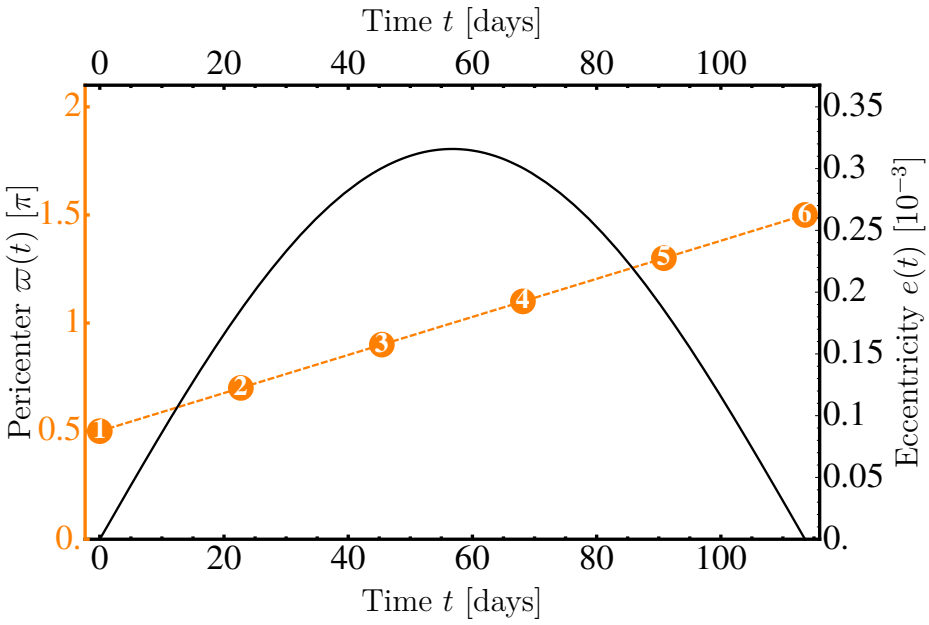

(a) Dynamical evolution of pericenter and eccentricity

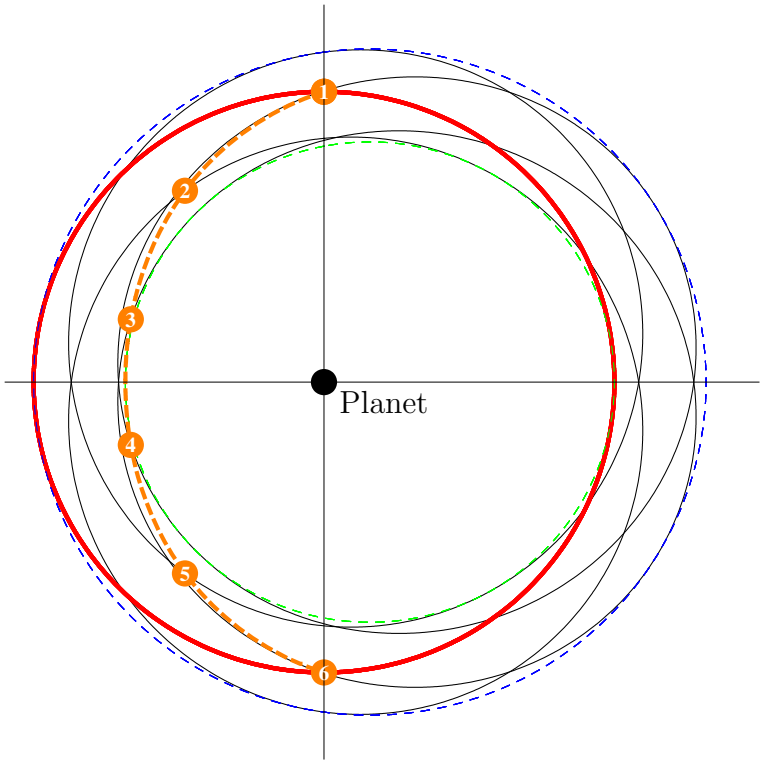

(b) Annulus generation in physical space

Figure 3.2 The upper panel **(a)** shows the dynamical evolution of the orbit elements, assuming a nominal grain of radius size $s = 33\,\mu$m in orbit about Saturn with semi-major axis $a = 2.21\,R_{\text{Saturn}}$ and zero initial eccentricity. The lower panel **(b)** depicts several orbits (black) for the nominal grain at different phases of the precession cycle, whereas the red, solid circle indicates the semi-major axes of the particles. The Sun is located on the right side of the page, i.e., the solar flux travels from right to left. In the lower panel, the eccentricity has been scaled by a factor of 10^3. The orange, numbered points correspond to the subsequent time steps of panel **(a)** and indicate the actual longitude of pericenter. Having a myriad of nominal grains on different phases of the precession cycle produces an annulus, which is shifted sunward. The annulus itself can be described by two enclosing ellipses (inner: green, dashed; outer: blue, dashed).

3.3.2. Heliotropicity - The Peculiar Orientation

The ringlet itself can be understood as being formed by a superposition of heliotropic annuli created by particle ensembles of different sizes s. The origin of an heliotropic annulus stems from the precession of the longitude of pericenter in conjunction with symmetric eccentricity gain and loss due to radiation pressure. This produces a sunward shifted eccentric annuls for a given grain size ensemble with phases distributed over the whole precession cycle of the pericenter. From symmetry in the dynamics one can conclude, that the orientation of an annulus is independent of particle characteristics. Indeed, weighting the longitude of pericenter ϖ (Eq. (3.23)) with the corresponding eccentricity e (Eq. (3.22)) and averaging over the cycle of pericenter precession yields an estimate for the mean longitude of pericenter

$$\varpi^{\dagger} \equiv \frac{\langle e\varpi \rangle_{\gamma}}{\langle e \rangle_{\gamma}} = \pi, \tag{3.34}$$

with

$$\langle \cdot \rangle_{\gamma} \equiv \frac{1}{2\pi} \int_{0}^{2\pi} \mathrm{d}(\gamma t/2) \ \cdot . \tag{3.35}$$

Hence, as long as the position of pericenter is constantly spinning around the planet, causing oscillatory changes in eccentricity, heliotropicity of an annulus is unaffected by the size or charge of the particle. This sort of averaging is based on the assumption, that a myriad of particles with radius size s at different phases of longitude of pericenter and corresponding eccentricity contribute to form an annulus.

For the sake of understanding, we note, that *anti-heliotropicity* is established by an inverse solar flux, by inverse precession of the pericenter, i.e., the pericenter moves towards local noon of the planet, or, by retrograde orbits of dust material around such a planet with corresponding pericenter motion. If the inclination is non-zero, there is also the regression of the longitude of ascending node (Ch. 2.1.1). In this case, regression of the longitude of ascending node and advance of the longitude of pericenter compete, which might also result in an anti-heliotropicity or even locked pericenter (Burns et al., 2001). The latter case would immediately imply arbitrarily large eccentricities, or to put it differently, particle removal.

3.4. Observations

Now that we have understood the special orientation, we are left to examine further consequences for observations of such heliotropic ringlets. From the number density in space, we may estimate optical quantities given by the heliotropic dynamics, which can be directly related to Cassini observations.

3.4.1. Dynamical Density In The Ringlet Region

To derive a dynamical density in the ringlet region, we neglect particle gains and losses, assuming the ringlet material to be in equilibrium and long-living with respect to the timescales of eccentricity and pericenter motion. The full problem of kinetics under dynamics (Boltzmann-equation) is broken down by timescale arguments, which allows a separate treatment of (heliotropic) kinematics and kinetics, i.e., gain and loss modeling (see Ch. 4).

We use the heliotropic dynamics, to derive a particle density, which in turn can be related to the optical depth (measurable quantity) of the ringlet. We therefore assume, that the number of streamlines at a given position (r,φ) in space corresponds to the dynamical number of particles. By this, we equally spread the mass of each individual grain over its streamline. Since small eccentricities can be assumed ($e \ll 1$), the streamline of a particle is given by the simplified version of Eq. (3.29)

$$\tilde{r}(\varphi,\varpi) \cong a(1 - e\cos(\varphi - \varpi)). \tag{3.36}$$

Dynamically, the number of streamlines at position (r,φ) of size s, having all semi-major axis a is given by

$$n(r,\varphi,s,a) = C_0 \int_{\pi/2}^{3\pi/2} \mathrm{d}\varpi\, \delta(r - \tilde{r}(\varphi,\varpi)), \tag{3.37}$$

with normalization constant C_0, which allows to set the right units and scaling. The Dirac-Delta function $\delta(r - \tilde{r}(\varphi,\varpi))$ ensures, that all streamline contributions to the number of particles at position (r,φ) are counted. Note that Eq. (3.37) does not account for the motion of pericenter $\dot{\varpi}$ and the particle itself. The former effect would slightly change the contributions of streamlines along the integration of ϖ, since $\dot{\varpi}$ implies rotating ellipses. The latter implies a non-homogeneous mass distribution along the streamline, which results into symmetric $n(r,\varphi,s,a)$ around the initial

starting points (Horanyi et al., 1992). Indeed, the motion of the particle depends on its azimuthal position, i.e., a particle spends more time around apocenter than at pericenter, while at the same time, apocenter particles are more spread over a proportionally larger annulus. Both effects exactly balance each other, to produce symmetric $n(r,\varphi,s,a)$. Integration of equation (3.37) yields

$$n(r,\varphi,s,a) = \frac{C_0}{a\, e_{\max}\sqrt{1-\left(\frac{2(r-a)}{a\, e_{\max}} - \cos\varphi\right)^2}}. \tag{3.38}$$

The number of streamlines $n(r,\varphi,s,a)$ can be interpreted as a measure for the particle occurrence at a given point normalized to the annulus area, which is created by the particle ensemble. Thus, we refer to $n(r,\varphi,s,a)$ as the number density of particles in the following, by choosing C_0 in such a way, that $n(r,\varphi,s,a)\, r\mathrm{d}\varphi\mathrm{d}r$ becomes the vertically integrated number of particles at (r,φ) in the area increment $r\mathrm{d}\varphi\mathrm{d}r$. It is of crucial importance, not to confuse this density with the classical streamline density, which is a complete different measure (e.g. Showalter et al., 1986).

From Eq. (3.38), we find more particles at the radial turning points (Fig. 3.3). This is an analogous behavior to a pendulum of a pendulum clock, which spends most of its time at the turning points. Note, the same result could have been obtain by the fact, that the dynamical density is proportional to the inverse of the radial velocity times radial distance (e.g. Horanyi et al., 1992), which also accounts for the particles speed, producing symmetric dynamical densities.

3.4.2. Photometric Measurements

Images of the ringlet are based on absorbed, reflected, and transmitted light, either coming from the Sun or other light sources. Based on these images, photometric quantities can be derived, which in turn give clues about particle composition and dynamics of a ringlet or ring, respectively. Most commonly used quantity in photometry is the ratio of intensity of light I/F, which measures the ratio of a body's detected brightness I (power per area per wavelength interval per steradian) at a given phase angle to that of the incoming solar flux density πF (power per area per wavelength interval) and can be directly probed by occultation experiments. The phase angle α is defined as the angle between light source, object, and observer. Using the ratio I/F is very convenient, since spectral effects from the Sun's light flux and its distance from the rings are removed. At normal incidence, I/F equals unity for a perfectly diffusing *Lambert* surface.

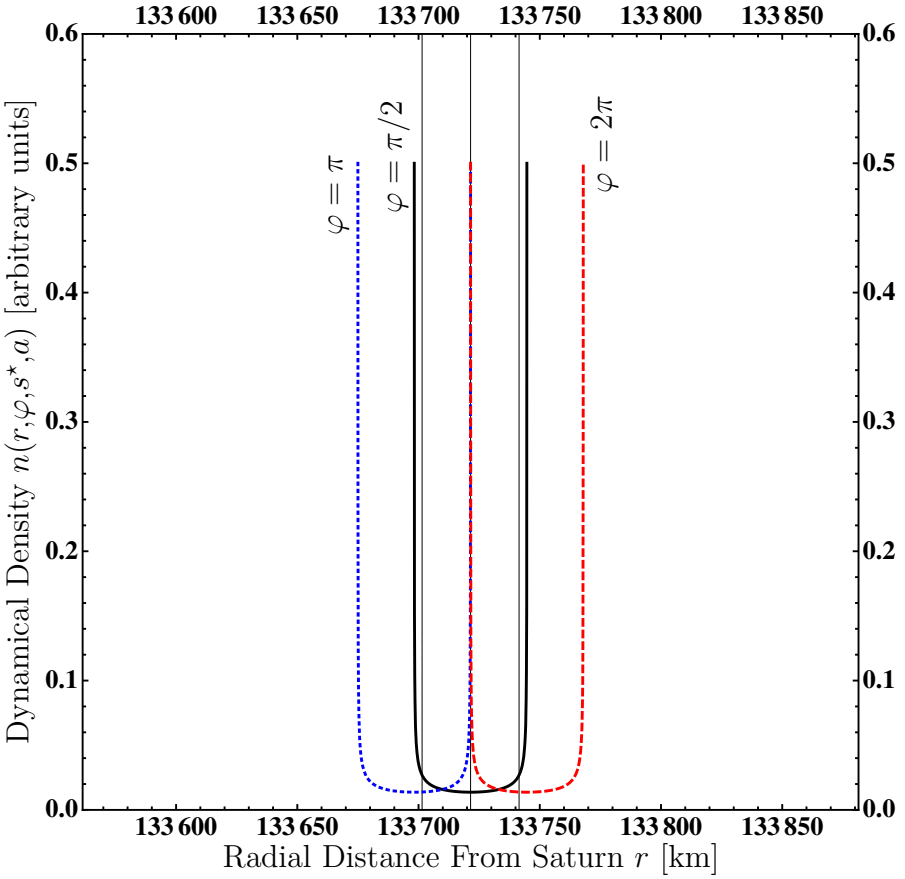

Figure 3.3 Dynamical particle density in arbitrary units as a function of radial distance evaluated around Saturn's Encke gap, using a nominal grain size of $s^\star = 30\mu$m with semi-major axis $a = 2.21\,R_{\text{Saturn}}$. The three curves correspond to the lateral ($\varphi = \pi/2$), local noon ($\varphi = 2\pi$) and midnight position ($\varphi = \pi$) at Saturn. Apparently, particles spend most of their time at their radial turning points, analog to a pendulum. All cuts are asymmetric, since we have neglected the speeds of the particles on the streamlines, hence, assuming equally distributed particles over the streamlines, when deriving the dynamical density. This is why at $\varphi = \pi, 2\pi$, we find a diverging density at a. The dynamical density is normalized to have unit area and clipped, owing the fact to be ill-defined at the turning points. The three vertical lines indicate the a (center) and extend to Pan's characteristic range of gravitational influence, i.e., *Hill radius* h_{Pan}.

Closely related to I/F is the optical depth τ, which describes how much absorption and scattering occurs, when light travels through a medium and directly reflects particle properties. For reasonably low optical depths, $\tau \ll 1$, I/F and τ are related via (Burns et al., 2001)

$$\frac{I}{F} = \frac{\tau \zeta_0 P(\alpha)}{4\varsigma}, \tag{3.39}$$

where ς is the cosine of the emission angle measured from the ring normal vector to the line of sight, ζ_0 is the single scattering albedo, and $P(\alpha)$ is the phase function with phase angle α. Scattering albedo as well as phase function can for instance be derived from Mie theory and reflect averages over the particle size distribution. The single scattering albedo represents the fractional amount of impinging light, which is not absorbed by the particle. Its range lies between zero and one. The phase function describes the fraction of light scattered into a given direction. It is normalized to give an average value of unity, when integrating over all solid angles.

The *normal* $\tau \equiv \varsigma\tau$ of a heliotropic ringlet, i.e., the optical depth seen perpendicular to the ringlet, is given by

$$\tau(r,\varphi) = C_1 \int \mathrm{d}s\, \tau_s(s,r,\varphi) N(s), \tag{3.40}$$

with normalization constant C_1 and individual annuli contributions

$$\tau_s(s,r,\varphi) = \sigma(s) Q_{eff}(s,\lambda)\, n(r,\varphi,s). \tag{3.41}$$

We shall make a series of comments on this.

The basic idea of this procedure is to multiply the size dependent normal optical depth of every annulus with its number of occurrence, i.e., number of particles having size s, and sum over the resulting individual optical depths. The individual annuli contributions are given by particle cross-section $\sigma(s) = \pi s^2$, scattering efficiency factor Q_{eff}, vertically integrated dynamical particle density $n(r,\varphi,s) = \int \mathrm{d}z\, n_z(z,r,\varphi,s)$, which we take from Eq. (3.38), since we want to investigate optical properties, that arise from heliotropic dynamics.

In general, Mie theory is employed to derive the relation between Q_{eff} and particle size s as well as the wavelength λ of the light. For micron sized dust grains, it is convenient to introduce the dimensionless size parameter $X \equiv 2\pi s/\lambda$. For X of the order of unity, Q_{eff} is of order unity, decreasing rapidly for smaller X; typically $\propto X^4$ (Burns et al., 2001). For large X, Q_{eff} approaches 2, which reflects Babinet's principle. We assume $Q_{eff} = 1$, for all particles sizes in the micron range, which is a fair approximation for wavelengths in the visible part of the solar spectrum.

In order to model the optical depth of the ringlet, information about the particle size distribution $N(s)$ is required, which we assume to be mainly determined by the particle source mechanisms. A potential particle source mechanism is given through constant bombardments of source bodies with micrometeoroids (Krüger et al., 2000). From this model one expects a power law for the particle size distribution $N(s)$ with

slope $q \approx 3$,

$$N(s) \propto (1/s)^3 \quad s_{\min} < s < s_{\max}. \tag{3.42}$$

Note, this choice is generally non-unique, when deriving the particle size distribution from photometric measurements (Burns et al., 2001). However, for the Encke gap, we can already constrain the minimal size $s_{\min}$ from Eq. (3.25). Assuming the micrometeoroid flux model, the maximal grain size $s_{\max}$ can be approximated by the biggest micrometeoroids (Krivov et al., 2003, Spahn et al., 2006). This approximation of maximal grain size is motivated by an energetic argument, i.e., it is very unlikely, that particles larger than the impacting ones (radii of about 100 microns) are produced during the impact. These choices are in full agreement with observations and related photometric modeling for heliotropic ringlets (Hedman et al., 2007), from which a particle size range of $1 - 100$ microns is expected.

To test our heliotropic model against observations, especially the heliotropic eccentricity and the ringlet-width, we calculate the normal optical depth (3.40) of a ringlet, placed into the center of a gap, i.e., semi-major axis of the particles lies in the center, by assuming the size distribution (3.42), and find

$$\tau(r,\varphi,a) = C_2 \frac{s_{\max}^4 s_{\min}^4}{s_{\max}^4 - s_{\min}^4} \frac{\arcsin\left(x_{\max}(r,\varphi,a)\right) - \arcsin\left(x_{\text{low}}(r,a,\varphi)\right)}{2(r-a)}, \tag{3.43}$$

with normalization constant C_2, which has to be chosen in such a way, that $\tau(r,\varphi,a)$ becomes dimensionless, and

$$x_{\max}(r,\varphi,a) = \frac{2(r-a)}{e_c a} \frac{s_{\max}^\star}{s_{\min}} - \cos\varphi \tag{3.44}$$

$$x_{\min}(r,a,\varphi) = \frac{2(r-a)}{e_c a} - \cos\varphi, \tag{3.45}$$

whereas the position dependent (indicated by *) upper grain size limit $s_{\max}^\star$ reads

$$s_{\max}^\star = \begin{cases} s_{\max}\Theta(s_1^\star - s_{\max}) + (s_1^\star\Theta(s_1^\star - s_{\min}) + s_{\min}\Theta(s_{\min} - s_1^\star))\Theta(s_{\max} - s_1^\star) & : \text{I} \\ s_{\max}\Theta(s_2^\star - s_{\max}) + (s_2^\star\Theta(s_2^\star - s_{\min}) + s_{\min}\Theta(s_{\min} - s_2^\star))\Theta(s_{\max} - s_2^\star) & : \text{II}, \end{cases} \tag{3.46}$$

distinguishing cases $\text{I} : 0 < r \leq a$ and $\text{II} : 0 < a < r$. $\Theta(x)$ represents the Heaviside

function defined as

$$\Theta(x) = \begin{cases} 0 & x < 0 \\ 1 & x \geq 0. \end{cases} \tag{3.47}$$

Finally, we have

$$s_1^\star = s_{\min} \frac{e_c a}{2(a-r)}(1 - \cos\varphi), \tag{3.48}$$

$$s_2^\star = s_{\min} \frac{e_c a}{2(r-a)}(1 + \cos\varphi), \tag{3.49}$$

and the critical eccentricity e_c, which comes from the parametrization of the maximal eccentricity (Eq. (3.26)),

$$e_c = \frac{p}{2a}, \tag{3.50}$$

assuming circular shapes of the gap edges and a finite gap width p. Figure 3.4 illustrates the spatial dependence of the upper size limit (Eq. (3.46)).

These parameters arise from the position-dependence of the grain size limits. At any azimuthal position there is a radial window of half of the gap width, to which particles on eccentric orbits, and hence their streamlines, are constrained. This is taken into account by Eq. (3.46), setting the upper grain size limit to that of the smallest grain size, outside the radial window, which in turn produces zero contribution to the normal optical depth.

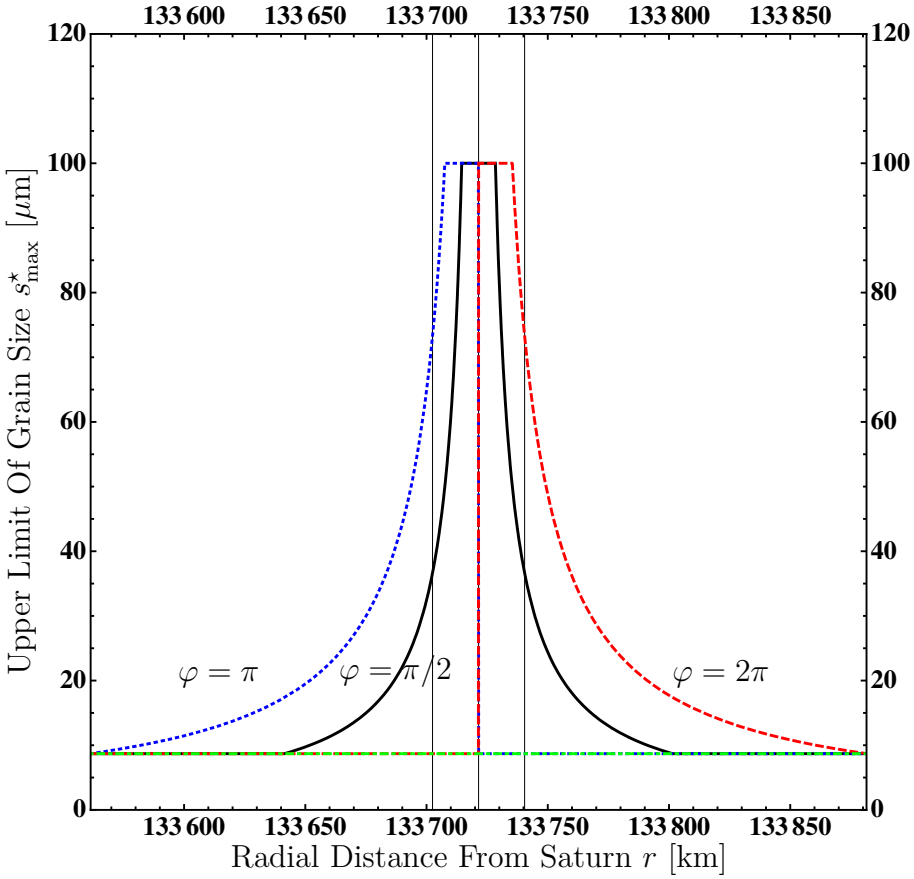

Figure 3.4 Spatial dependence on the upper limit of the grain size, evaluated for different azimuthal positions at the Encke gap. The abscissa - radial position - spans the whole gap width. The lower green, dashed line corresponds to the smallest possible grain size. Also visible is the radial window - intersections of the $s^{\star}_{\max}$ curves with the lower green, dashed line - of about 160 km width, which corresponds roughly to half of the Encke gap. The three vertical lines indicate semi-major axis a (center) and extend to Pan's characteristic range of gravitational influence, i.e., *Hill radius* $h_{\mathrm{Pan}} \approx 19$ km.

3.5. Application To The Central Ringlet In The Encke Gap

The critical eccentricity for particles in the central ringlet evaluates to $e_c \approx 1.2 \cdot 10^{-3}$, which - from relation (3.25) - translates into a minimal grain size of $s_{\min} \approx 8.7$ microns. The maximum grain size is taken to be $s_{\max} = 100$ microns. Figure 3.5 shows the normal optical depth from equation (3.43) for different azimuthal positions, upper panel **(a)**. The lower panel **(b)** shows the normal optical depth, averaged over the semi-major axes, indicated by $\langle\rangle_a$, which should be closer to the physics of "smeared" semi-major axes. Consequently, the average is taken in the range $a \pm \mathrm{h}_{\mathrm{Pan}}$, with equally distributed semi-major axes, reflecting the belt of source moonlets, which is

restricted to Pan's horseshoe region. Here, $h_{\mathrm{Pan}} \approx 19$ km is Pan's characteristic range of gravitational influence, i.e., *Hill radius*, with mean distance of Pan from Saturn $a = 2.21\, R_{\mathrm{Saturn}}$. We do not consider variations of ϖ with semi-major axes, while averaging, since they are negligible small. All curves are measured per unit area.

Naively, from Fig. 3.3 one would expect to get a mean U-shaped-like profile. Indeed, this is the case for a constant particle size distribution ($N(s) = const. = s_{\max}$), visible in Figs. 3.4 and 3.5 **(a)** and assumed for radial range

$$r \in \left[\frac{a}{2}\left(e_{\max}(s_{\max})(\cos\varphi - 1) + 1\right), \frac{a}{2}\left(e_{\max}(s_{\max})(\cos\varphi + 1) + 1\right)\right]. \tag{3.51}$$

Outside this range, the optical depth drops, simply because larger particles become more and more depleted, since they are rather concentrated to the center of the ringlet.

Besides the explained peculiar orientation, there are two additional important outcomes of our annulus ringlet model compared to observations (Ferrari and Brahic, 1997, Hedman et al., 2007), i.e., the apparent eccentricity of the ringlet and the ringlet-width.

3.5.1. Apparent Eccentricity Of The Ringlet

To measure the ringlet's eccentricity, we use the radial shifts in Fig. 3.5, as well as the averaged eccentricity from Eq. (3.22) according to

$$e_{\mathrm{ringlet}} \equiv \langle e \rangle_{s,\gamma} \tag{3.52}$$

with

$$\langle \cdot \rangle_{s,\gamma} = \frac{\int \mathrm{d}s\, \langle \cdot \rangle_{\gamma}\, \sigma(s) N(s)}{\int \mathrm{d}s\, \sigma(s) N(s)}, \tag{3.53}$$

particle cross-section $\sigma(s) = \pi s^2$, particle size distribution $N(s)$, and $\langle \cdot \rangle_{\gamma}$ from Eq. (3.35). The limits of the size integration are given by the particle size distribution. Note, the average over the particle sizes (3.53) accounts for the number of occurrence and weights also the visibility in the observation data via the particle cross-section. This average should be somewhat closer to observations than a simply average over the particle size distribution. The *apparent* particle size distribution is then $\propto s^{-q+2}$, which effectively makes the ringlet heavier, since larger particles are favored more with respect to the size distribution (3.42). Further on, the apparent ringlet eccentricity is pushed down, since larger dust grains have smaller eccentricities.

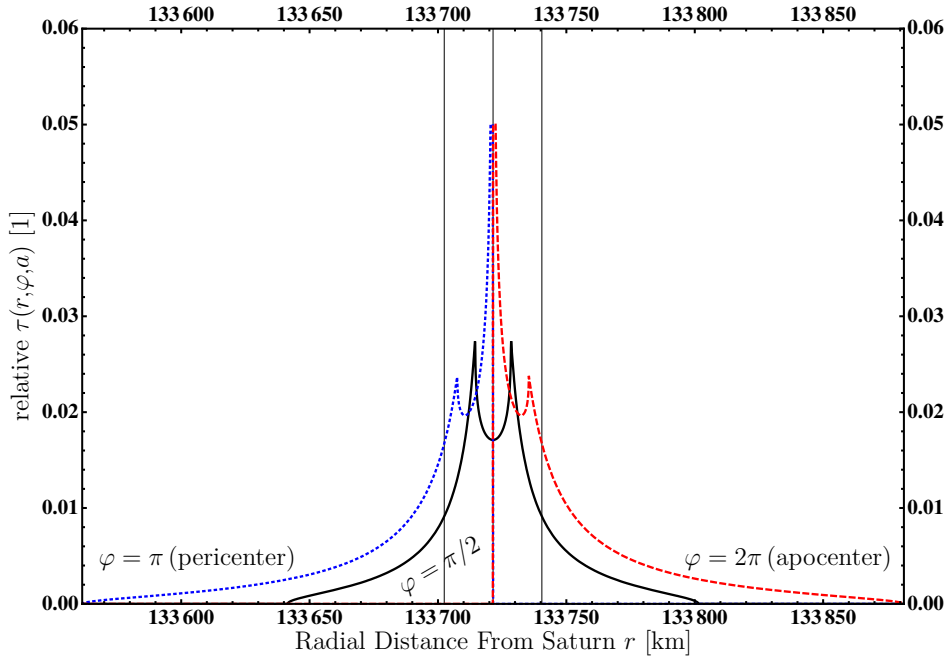

(a) Normal optical depth (in arbitrary scale) produced by particles on circular orbits about Saturn with $a = 2.21\,R_{\text{Saturn}}$.

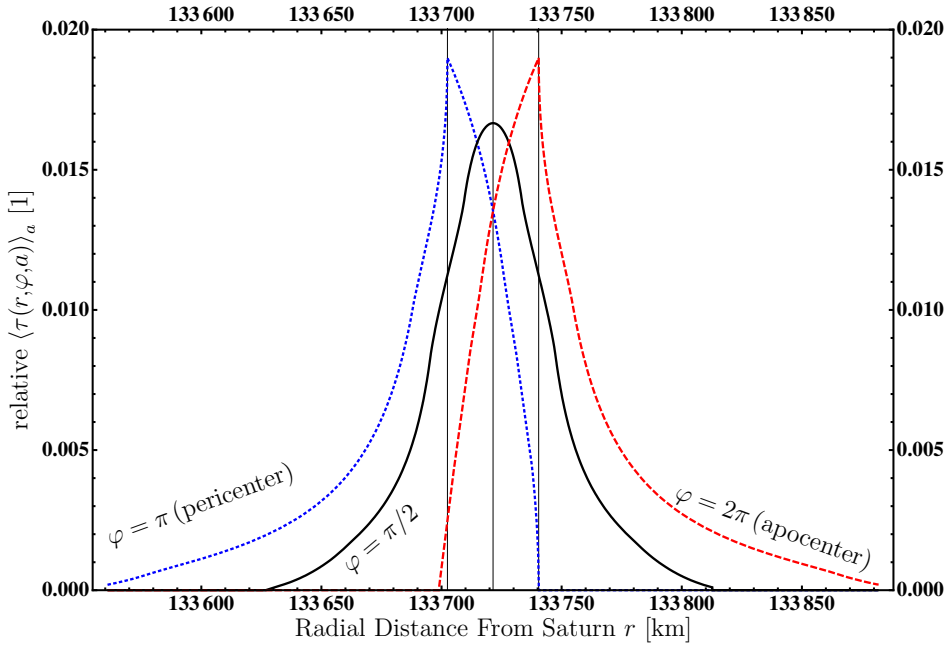

(b) Normal optical depth (in arbitrary scale) produced by particles on circular orbits about Saturn with $a = 2.21\,R_{\text{Saturn}} \pm h_{\text{Pan}}$.

Figure 3.5 Normal optical depth for **(a)** particles on circular orbits at $a = 2.21\,R_{\text{Saturn}}$ and **(b)** numerically averaged over equally distributed semi-major axes $a = 2.21\,R_{\text{Saturn}} \pm h_{\text{Pan}}$. All curves are normalized to have same areas. In panel **(a)** the bump in the curves comes from the shape of the dynamical density. In this region, all particle sizes are allowed, whereas in the other region, the contribution by large particles vanishes and approaches the minimal grain size (Fig. 3.4). In both plots, the helitropicity is evident by the radial shift away-from/towards Saturn at local noon/midnight (apo-/pericenter) position, respectively, in our frame of reference. The three vertical lines indicate semi-major axis a (center) and extend to Pan's characteristic range of gravitational influence, i.e., *Hill radius* h_{Pan}.

To fix ideas, we use the particle size distribution from Eq. (3.42), when explicitly averaging over particle sizes in the following subsections. We further neglect the Lorentz contribution by setting $\gamma \equiv \varpi_{J_2}$, which makes γ independent of the grain size s, and define the particle size ratio $\xi \equiv s_{\max}/s_{\min}$. Then, the apparent eccentricity of the ringlet reads

$$e_{\text{ringlet}} = \frac{2}{\pi} e_{\max}(s_{\max}) \frac{\xi - 1}{\log \xi}, \tag{3.54}$$

with limits ($s_{\max}$ fixed)

$$\lim_{\xi \to 1} e_{\text{ringlet}} = \frac{2}{\pi} e_{\max}(s_{\max}) \tag{3.55}$$

and

$$\lim_{\xi \to \infty} e_{\text{ringlet}} = \infty. \tag{3.56}$$

These limits illustrate the heliotropic physics going on. In the latter case, arbitrarily small particles may contribute to the mean eccentricity, which of course diverges $\propto 1/s_{\min}$, the scaling of solar radiation pressure with grain size (Sec. 2.2.2). Note, these limits are only valid, if the Lorentz force is neglected. Especially in the case of $\xi \to \infty$, we would find different limits, depending on the sign of the surface potential, since the Lorentz force is capable of influencing the maximal eccentricity via the precession rate of the pericenter.

Evaluation at the center of the Encke gap yields $e_{\text{ringlet}} \approx 2.4 \cdot 10^{-4}$. From the optical depths in Fig. 3.5 we have in panel **(a)** / **(b)** radial shifts of $\Delta r \approx 13\,km$ / $\approx h_{\text{Pan}}$, which correspond to eccentricities of $e_\tau \approx 1 \cdot 10^{-4}$ / $\approx 1.4 \cdot 10^{-4}$. In panel **(a)** we use the radial shift of the bump, in panel **(b)** the maximum of the optical depth. Both values fit fairly well the observations (Ferrari and Brahic, 1997, Hedman et al., 2007), which report eccentricities around $e \approx 1 \cdot 10^{-4}$ and $\approx 2 \cdot 10^{-4}$, respectively. The semi-major axis scaling is $e_{\text{ringlet}} \propto a^4$ and stems from stronger gravity and planetary oblateness perturbations of the central planet. Particles move faster the closer they get to the central planet. Additionally, their precession rates of pericenter speed up. In the picture of orbit-averaged motion, both accelerations result into a smaller maximal eccentricity, which a grain of given size can obtain from solar radiation pressure.

3.5.2. The Narrow Ringlet-Width

As shown in Fig. 3.2 **(b)**, the initial infinitesimal ringlet-width $w_{\text{ini}} = 0$ km at radial position $r = a$ - particles start on circular orbits (red circle) - broadens to an apparent width (black ellipses), under the influences of solar radiation pressure and precessions of the pericenters. This width can be quantified by the *distance between enclosing ellipses*, *eccentricity dispersion*, *full-width-at-half maximum* of the optical depth profile (FWHM), and *maximal eccentricity*.

3.5.2.1. Distance Between Enclosing Ellipses

In Fig. 3.2 **(b)** we have depicted the enclosing ellipses, that envelope the annulus (green and blue dashed lines). From Eqs. (3.31), (3.32) we calculate the distance between those two ellipses for every grain size s and average over the grain sizes, which provides us a measure of the ringlet-width. The distance $\Delta r(s)_{\text{enclose}}$ between the enclosing ellipses at pericenter of the outer and apocenter of the inner one ($\varphi = \pi$) is given by

$$\Delta r(s)_{\text{enclose}} = a e_{\max}(s). \tag{3.57}$$

Defining the apparent ringlet-width based on the enclosing ellipses we have

$$w_{\text{enclose}} \equiv \langle \Delta r(s)_{\text{enclose}} \rangle_s = a \langle e_{\max}(s) \rangle_s \tag{3.58}$$

with size average

$$\langle f \rangle_s = \frac{\int \mathrm{d}s\, f\sigma(s)N(s)}{\int \mathrm{d}s\, \sigma(s)N(s)}, \tag{3.59}$$

whereas f is an arbitrary function $f(s)$, $\sigma(s) = \pi s^2$ is the particle cross-section and $N(s)$ the particle size distribution (Eq. (3.42)). The size average of the eccentricity in Eq. (3.58) yields

$$\langle e_{\max}(s) \rangle_s = e_{\max}(s_{\max}) \frac{\xi - 1}{\log \xi}, \tag{3.60}$$

where the Lorentz force contribution has been neglected. The limits for fixed $s_{\max}$ read

$$\lim_{\xi \to 1} \langle e_{\max}(s) \rangle_s = e_{\max}(s_{\max}) \tag{3.61}$$

and

$$\lim_{\xi \to \infty} \langle e_{\max}(s) \rangle_s = \infty, \tag{3.62}$$

reflecting the physics, that the ringlet-width is given by eccentric dust grains, whereas the eccentricity is inversely proportional to the grain size. In the former case ($\xi = 1$), only grains of size $s = s_{\max}$ are present in the ringlet, producing only one annulus of width $w_{\text{enclose}} = a e_{\max}(s_{\max}) \approx 14$ km. Here the right-hand-side term is evaluated for the central ringlet of the Encke gap. This sets the lower ringlet-width limit of our annulus model. With the presumed size distribution (3.42) and the ringlet-width measure of radial distance between enclosing ellipses, we cannot produce thinner heliotropic ringlets than this!

From the definition of $e_{\max}(s)$ we find, that heliotropic ringlet-widths in Saturn's ring system at position a are roughly given by

$$w_{\text{enclose}} \approx 0.26 \cdot \left(\frac{a}{R_{\text{Saturn}}} \right)^5 \frac{\xi - 1}{\log \xi} \text{km}, \tag{3.63}$$

assuming $s_{\max} = 100\,\mu$m.

For the central Encke gap ringlet, this evaluates to $w_{\text{enclose}} \approx 60$ km. Observations report ringlet-width of about 10 to 23 km (Ferrari and Brahic, 1997, Murray and Dermott, 2000, personal communication M. M. Hedman), which differs by a factor of about 3 to 6 from the ringlet-width based on the enclosing ellipses. To equate observations with this ringlet-width measure w_{enclose}, the lower size limit should be at least $s_{\min} \geq 39\mu$m, with power law slope $q = 3$. Note that Eq. (3.63) gives the possibility to get hints about the particle size distribution (e.g. for an assumed power law one could obtain slope q and the boundaries $s_{\min}$, $s_{\max}$), by directly measuring the ringlet-width in the Cassini data.

For fixed ξ, Eq. (3.63) implies, that ringlet-widths become smaller with decreasing semi-major axis, since the scaling is $\propto a^5$, which can be split into two contributions. The linear a contribution stems from smaller radial excursion of eccentric particles, closer to the central planet. The additional a^4 contribution is due to the eccentricity scaling (Sec. 3.5.1).

3.5.2.2. Eccentricity Dispersion

The eccentricity dispersion is given by

$$\delta e \equiv \sqrt{\langle e^2 \rangle_{s,\gamma} - \langle e \rangle_{s,\gamma}^2}. \tag{3.64}$$

From Eqs. (3.22) and (3.53) we have

$$\delta e = \frac{2}{\pi} e_{\max}(s_{\max}) \sqrt{\frac{\pi^2}{16} \frac{(\xi^2 - 1)}{\log \xi} - \left(\frac{\xi - 1}{\log \xi} \right)^2}. \tag{3.65}$$

For fixed $s_{\max}$, the limits of δe read

$$\lim_{\xi \to 1} \delta e = \frac{2}{\pi} e_{\max}(s_{\max}) \sqrt{\pi^2/8 - 1} \tag{3.66}$$

and

$$\lim_{\xi \to \infty} \delta e = \infty. \tag{3.67}$$

Based on the eccentricity dispersion, we can define a measure for the ringlet-width-variation, i.e.,

$$\delta[w] \equiv 2a\delta e, \tag{3.68}$$

Assuming $s_{\max} = 100\,\mu$m, heliotropic ringlet-width-variations in Saturn's ring system at position a are roughly given by

$$\delta[w] \approx 0.33 \cdot \left(\frac{a}{R_{\text{Saturn}}} \right)^5 \sqrt{\frac{\pi^2}{16} \frac{(\xi^2 - 1)}{\log \xi} - \frac{(\xi - 1)^2}{(\log \xi)^2}}\,\text{km}. \tag{3.69}$$

For the center ringlet of the Encke gap, we have $\delta e \approx 2.5 \cdot 10^{-4}$, which corresponds to a ringlet-width-variation of about $\delta[w] \approx 67.9$ km.

3.5.2.3. The FWHM

Another measure for the ringlet-width is given by the FWHM, directly derived from the heliotropic optical depth. From Eq. (3.43) we numerically determine the FWHM for the central ringlet at azimuthal position $\varphi = \pi/2$ to about $w_{\text{FWHM}} \approx 26.4$ km. The FWHM of the semi-major axis averaged optical depth yields a somewhat larger value

of $w_{\mathrm{FWHM}} \approx 52$ km, still below the ringlet-width derived from the enclosing ellipses. This is due to the fact, that the FWHM is not that susceptible to the tails as is the average over the entire size ensembles.

3.5.2.4. Maximal eccentricity

When moving radially further out- or inward, the normal optical depth decreases gradually, until the edges of the radial window of allowed dust grains are passed (see Figs. 3.5 and 3.6). However, the Encke gap ringlet is reported to be very confined (Porco et al., 2005, personal communication M. M. Hedman and J. A. Burns) within the measured ringlet-widths, implying a sharp drop-off within hundreds of meters or even less. Taking this as the measure, our model would yield a ringlet-width of about 160 km (radial window width), simply because the A ring edges constitute a sharp drop-off in the size distribution via absorption of dust grains with eccentricities larger than half of the gap width.

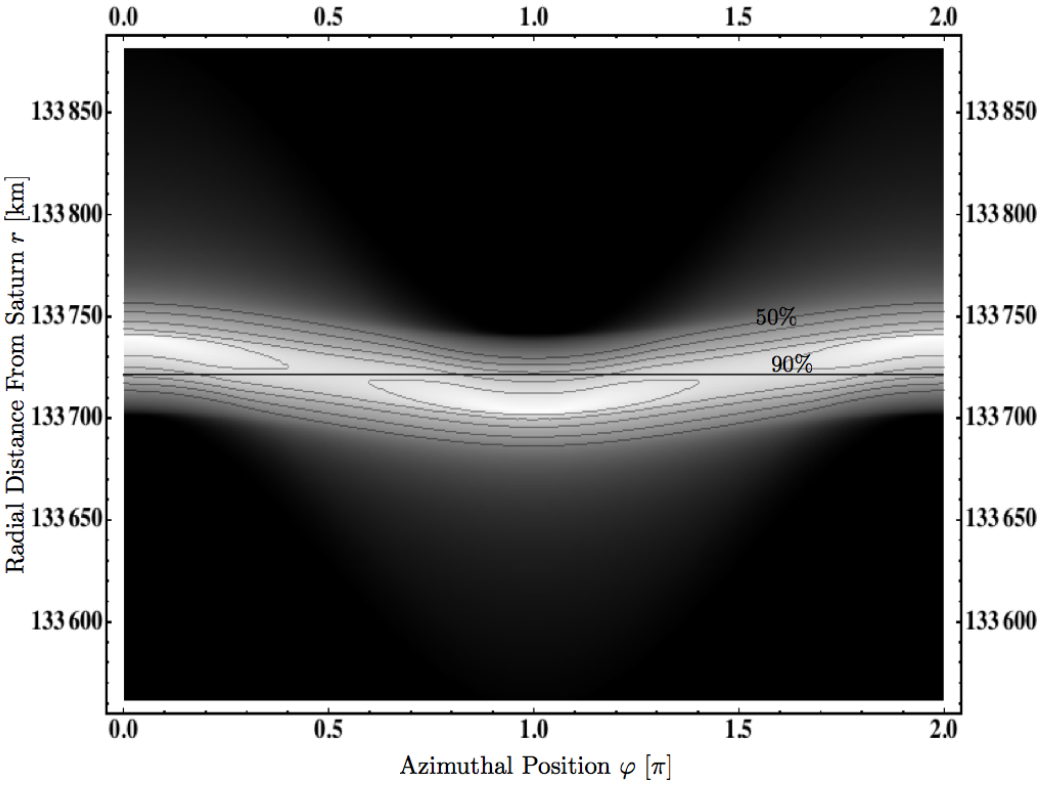

Figure 3.6 Normal - semi-major axis averaged - optical depth of the central Encke gap ringlet as a function of radial and azimuthal position with linear gray scale. The black line indicates the center of the ringlet, whereas the thin, gray lines represent isolevels of the maximum normal optical depth. The isoline increment is 10 % starting from 50 to 90 %.

These consistent overestimates of the ringlet-width by the annulus model are indicative for a size distribution that differs from the one being used (Eq. (3.42)). This is due to neglected mechanisms, that lead to various lifetimes for different grain sizes, which are directly related to the very confined ringlet. For instance, scattering of dust grains at moonlets embedded in the ringlet, especially those with semi-major axes close to the edge of the observed ringlet, could lead to the observed sharp drop-off (Spahn, 1987, Spahn and Sponholz, 1989, Hahn, 2006).

Notice that Pan itself cannot noticeably remove ringlet particles, which fulfill the critical eccentricity criterion, derived from the gap edges (Eq. (3.25)), if diffusive process are neglected (see Ch. 4). This can easily be shown by applying the encounter problem of Henon and Petit (1986). They investigate the circular Hill problem, which is the encounter version of the restricted circular three body problem, and derive an expression for the closest approach distance η between the guiding center of the test particle (horseshoe motion assumed) and the center of the moon. The guiding center refers to the mean circular orbit of a particle, on which the epicyclic motion - due to the particle's eccentricity - is superimposed. This is an approximation accurate to order e, and very useful for system, viewed in a corotating frame of reference. In a frame of reference that corotates with the satellite, the closest approach distance for a given impact parameter $b = \frac{|\Delta a|}{h_{\mathrm{Pan}}}$ reads (Henon and Petit, 1986, Ida and Nakazawa, 1989)

$$\eta = \frac{8}{b^2} h_{\mathrm{Pan}} \overset{b=1}{\underset{\downarrow}{\approx}} 160\,\mathrm{km}. \tag{3.70}$$

Pan itself extends almost to its Hill radius, so that one has to subtract $h_{\mathrm{Pan}} = 19$ km from the closest approach η, to get the closest possible collision-free approach of $\eta_{cf} = 141\,\mathrm{km}$, presuming the particle to have semi-major axis $a = a_{\mathrm{Pan}} \pm h_{\mathrm{Pan}}$. Note, this is a lower limit for particles in the ringlet region, since $\eta \propto 1/b^2$. Consequently, almost any configuration of impact parameter (= semi-major axis) and allowed eccentricity (Eq. (3.25)) within the horseshoe region of Pan ($a_{\mathrm{Pan}} \pm h_{\mathrm{Pan}}$) is unaffected by Pan. Small particles ($s < 13\,\mu$m), that have semi-major axes close to the edge of Pan's Hill sphere ($a = a_{\mathrm{Pan}} \pm h_{\mathrm{Pan}}$) and sufficiently large eccentricities, can be removed. This is of negligible amount (less than 2%, assuming the particle size distribution from Eq. (3.42) and semi-major axes equally distributed from $a_{\mathrm{Pan}} - h_{\mathrm{Pan}} < a < a_{\mathrm{Pan}} + h_{\mathrm{Pan}}$), since particles with allowed eccentricities and semi-major axes in the range $a_{\mathrm{Pan}} - 14\,\mathrm{km} < a < a_{\mathrm{Pan}} + 14$,km have collision-free closest approaches. On the other hand, embedded moonlets, which are sufficiently small to live on Pan's horsehoe

orbits but at the same time have enough mass to affect dust grains, could do the job by either scattering material directly out of the ringlet region or by pushing them into Pan's scattering zone.

Additional observatory facts, that also call for embedded moonlets, are the very kinky and clumpy structures as well as the strong azimuthal brightness variations of the Encke gap ringlets. The Encke gap ringlets are morphological very close to the F ring, Fig. 1.6. Murray et al. (2008) have recently shown, that shepherding of Pandora and Prometheus - two of Saturn's satellites - including embedded moonlets in the bright core of the F ring can account for the observed clumpy structures. In the case of the F ring, these structures vary on timescales of days, alarmingly close to those of heliotropic dynamics.

Another possibility to explain the narrow confined ringlet comes from the observation itself. Figure 3.6 illustrates a pol view of the ringlet (normal optical depth from Eq. (3.43)). The isolines of 50 to 100 % of the normal optical depth maximum form a very constrained ringlet. Usually, one has to remove a contamination level (=background) in the I/F data. A background level, which is above the I/F level produced by ringlet grains that lie radially around the tails of the optical depths, would produce a sharp edge. For instance, if the background level would be around 80% of the maximum of the heliotropic optical depth, a very confined ringlet of about 15 km width would be measured (Fig. 3.6). Notice the heliotropicity is easily seen at $\varphi = \pi$ and $\varphi = 2\pi$.

Finally we note, that mechanisms which decrease the maximal eccentricity of a dust grain, e.g., higher precession rate of the ringlet particles or smaller radiation pressure effects, cannot produce a nice drop-off at $10 - 20$ km ringlet-width, since eccentric particles would still fill half of the gap width. These mechanisms would only decrease the lower limit of the particle size distribution.

CHAPTER 4

The Sinks And Sources Of Dusty Ringlets

The annulus model has a slight deficit in describing the ringlet-width. This is most likely related to mechanism that have not been included into the model and possibly calls for strong grain size dependence on the lifetimes. The lifetime of each individual dust grain is given by dynamic as well as kinetic processes. So far we have been dealing with dynamics and related normal optical depth of the ringlet produced by a given particle size distribution. In this chapter we identify kinetic processes, that maintain the ringlet itself, influence lifetimes, and contribute to the particle size distribution.

4.1. Identification Of Possible Particle Sinks And Sources

4.1.1. Particle Sinks

We have already identified dynamical sinks for heliotropic ringlet particles in Ch. 3, i.e., gap edges and other potential celestial bodies, which remove particles from the ringlet via collisions. Moonlets embedded in the ringlet region would also serve as sinks, whereas Pan can be excluded, assuming horseshoe-like motion of the dust grains. This does not hold, if diffusive processes due to stochastic fluctuation (e.g. moonlet scattering, charge fluctuations, or radiative forces) drive ringlet particles into the scattering region of Pan.

Micrometeoroids have high relative velocities and - once striking a ringlet dust grain - are capable of immediately removing it from the ringlet region. Furthermore adhesion of colliding ringlet particles may preferentially remove smaller particles to form larger ones. Furthermore, even collisions among the ringlet particles may lead to fragmentation.

Besides dynamical sink mechanisms, dust grains suffer mass loss due to sublimation

and sputtering. The former sink being of negligible strength at Saturn's distance from Sun. The second sink mechanism can be split into plasma *sputtering* via energetic ions and electrons, and UV photon *sputtering*. *Sputtering* can be thought of micro-erosion, i.e., the impacting elementary particles alter a grain's chemical as well as structural composition, preferably on the surface, and lead to a successive desorption (Johnson, 1991, Strazzulla and Johnson, 1991).

4.1.2. Particle Sources

Already registered as a potential sink, micrometeoroid bombardment is also efficient in producing ringlet material, when projectiles impact onto a satellite's surface with relative high velocities of tens of kilometers per second. At the Encke gap, we have Pan and other putative embedded moonlets, that might supply the surface of impact.

The same impact mechanism onto embedded moonlets also holds for the ringlet particle itself, although orders of magnitude less efficient, due to small relative velocities of meters per second. Inter-moonlet-collisions might also supply ringlet material. Here, the efficiency is probably orders of magnitude below that of the micrometeoroid contribution, since again low relative velocities of meters per second are expected. Additionally, the dynamical optical depth of the moonlets is supposed to be small. Finally we also have contributions from inter-particle collisions, which potentially produces larger particles, while at the same time, removes the smaller ones. However, the contrary case can also not be excluded.

Concerning the micrometeoroid bombardment scenario, we note that Pan is a rather insufficient source. This is due to the fact, that almost all of the ejected material falls back onto the moon's surface. However, there are two positions in the vicinity of Pan, *Lagrange points* $\mathcal{L}_1$ and $\mathcal{L}_2$, at which the material can easily escape, since at these points, the combined gravitational accelerations of central planet and moon as well as the centrifugal forces acting on dust grains balance. Topologically, this results into two saddle-points, which separate regions of different kinds of motion of the dust grains (Fig. 2.3), i.e., orbits solely around the moon, horseshoe-like orbits around the central planet, or other non-classified types. We recall from Ch. 2, that these two points must be aligned with the central planet and the moon, whereas their separation from the moon is almost the moon's Hill radius.

Since Pan almost fills its entire Hill sphere, it is very unlikely, that particles can encircle Pan. So in order to get away from Pan, dust grains must pass one of the two Lagrange points. This in turn forces the ejected material on orbits, which have semi-major axes in the vicinity of Pan's Hill sphere. Spahn (1987) have shown, that

in this region, strong scattering occurs, so that most of the material, that has made it through $\mathcal{L}_{1/2}$, is scattered out of the ringlet region during the next encounter.

This qualitative reasoning is supported by numerical results from my colleague M. Makuch, which indicate that Pan's contribution to the ringlet material is evanescent small. In Fig. 4.1 we show the distribution of semi-major axes of particles (all of size $s = 37$ microns) after 10 days have elapsed from their launch of Pan, assuming the micrometeoroid bombardment scenario. Out of $N_i = 10^6$ starting particles, $4.2 \cdot 10^3$ particles can escape, but none of these has a semi-major axis within the Hill region of Pan. The semi-major axes of the remaining particles lie in the scattering region of Pan, so that with probability at least $\geq (1 - 1/N_i)$ ejected particles cannot contribute to the ringlet.

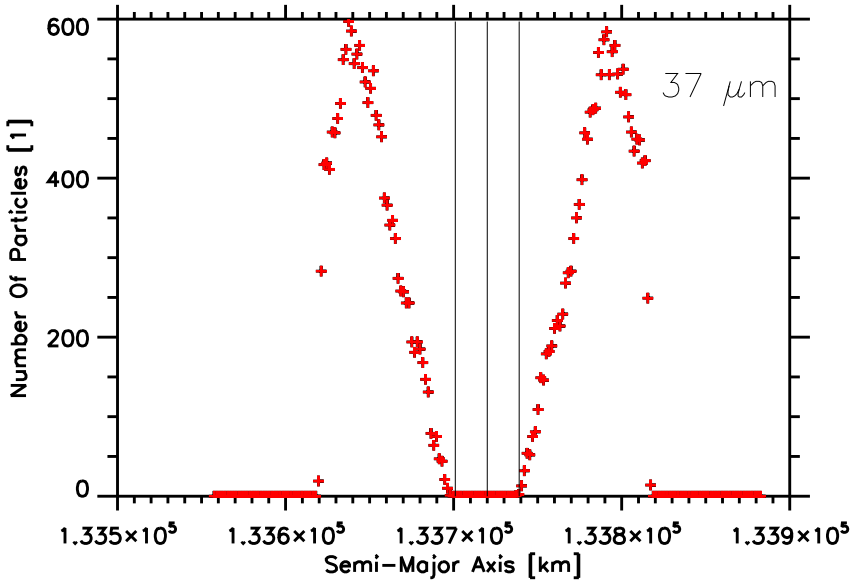

Figure 4.1 This plot shows the final semi-major axes distribution of nominal grains, having size $s = 37$ microns, which have been launched from Pan, according to the micrometeoroid bombardment scenario, and "survived" in the sense, that they did not fall back onto Pan nor did they hit the gap edges. The two vertical black lines, which surround a centered one (Pan's semi-major axis at 2.21 R_{Saturn}), represent part of Pan's Hill sphere ($h_{\text{Pan}} \approx 19$ km). Apparently, none of the particle has a semi-major axes within the Hill sphere of Pan, so that none out of these 10^6 particles can contribute to the central ringlet in the Encke gap. The simulations have been run for 10 days, without any of the perturbation forces we have considered, since none of these can potentially change the semi-major axis. Furthermore, particle orbits of the nominal grain size do not evolve to eccentricities, which might push the particles into the gap edges. Credit: M. Makuch, AGNLD Universität Potsdam

4.2. Feeding The Ringlet

4.2.1. Simple Kinetics

The evolution of the total number of particles N in the ringlet region can be described by the gain-loss master equation

$$\dot{N} = N^{+} - N^{-}, \tag{4.1}$$

where N^{+}, N^{-} represent particle gain and loss rates, respectively, averaged over the particle size distribution. If the loss rate is poorly known, it is possible to model the loss rate via an effective lifetime t_{life}, by assuming that the entire system has evolved to a steady state ($\dot{N} \equiv 0$) after the lifetime t_{life} has elapsed, i.e.,

$$N^{-} \simeq N^{+}\Theta(t - t_{life}). \tag{4.2}$$

Then, the solution of Eq. (4.1) takes the simple form

$$N = N^{+}\, t_{life} + N_0, \tag{4.3}$$

where N_0 represents the initial number of ringlet particles, which is assumed to be zero. The total number of particles N can be transformed into an optical depth, using the relation

$$\tau \equiv \frac{\sigma(s_{eff})N}{A}, \tag{4.4}$$

where the ringlet area is given by $A = 2a^2\pi e_{\tau}$,with estimated e_{τ} from Sec. 3.5.1. The effective particle size s_{eff} is obtained from the size average (Eq. (3.53)),

$$s_{eff} \equiv \langle s \rangle_s = s_{\min}\frac{\xi - 1}{\log \xi}. \tag{4.5}$$

Assuming $s_{\max}$ and $s_{\min}$ according to the dynamics in the Encke gap, we find an effective particle size of $s_{eff} \approx 37$ microns.

4.2.2. Application To The Encke Gap

The model parameters for the most sufficient source (micrometeoroid bombardment) are poorly constrained, i.e., the reported mass fluxes vary about 2 orders of magnitude.

It becomes even worse for the sink mechanisms. Although the main sinks are clear, there are little measurements, that can constrain the efficiencies of the various sinks. Therefore we adopt the adumbrated black box model for the sinks, based on an effective lifetime and a measured normal optical depth, which reflects an average over the entire particle size distribution in the ringlet. The gain rate is modeled by considering only the micrometeoroid bombardment scenario.

The optical depth is directly related to the source and sink mechanisms, since it is produced by material that has sufficient lifetimes to contribute to optical measurements. The ringlets in the Encke gap have large azimuthal brightness variations. Nevertheless, Porco et al. (2005) have determined a mean optical depth for the Encke gap ringlets of $\tau \approx 1.6 \cdot 10^{-2}$.

In this simple approach, the effective optical depth of the ringlet formed by particles having sizes s in the range $s \in [s_{\min} \dots s_{\max}]$ evolves according to (Eqs. (4.1)-(4.2),(4.4))

$$\dot{\tau} = \tau^{+}\, \tau_m \,(1 - \Theta(t - t_{life})), \tag{4.6}$$

where τ^{+} represents the optical depth gain rate of the ringlet given by the micrometeoroids that eject material from parent bodies, τ_m (m = moonlet). Assuming a steady state after the effective lifetime has elapsed, the loss term should be of the same order as the gain term. Note, Eq. (4.6) is averaged over the entire grain size distribution.

Following Krivov et al. (2003), the gain rate of the optical depth reads

$$\tau^{+} = \pi\, s_{eff}^{2}\, \frac{1-\alpha}{\alpha}\, \frac{M^{+}}{M_{max}} \left(\frac{M_{max}}{M_{min}}\right)^{\alpha}. \tag{4.7}$$

This represents a power-law with slope α, upper (M_{max}) and lower (M_{min}) mass limits of the cumulatively generated dust grains, that contribute to the optical depth. Reasonable slopes α vary in the range between 0.5 and 1 (see discussion in Krivov and Jurewicz, 1999). We assume $\alpha = 0.8$ (Krüger et al., 2000). The mass production rate M^{+} is given by

$$M^{+} = F_{imp} Y, \tag{4.8}$$

where F_{imp} gives the mass flux of impactors, taking into account gravitational focusing by the planet and scales according to $F_{imp} \propto v_{imp}$, the impact velocity of the micrometeoroids corrected by gravitational focusing effects. The ejecta yield Y, defined as the ratio of the total ejecta mass to the mass of impactors, scales like $Y \propto v_{imp}^{2.5}$ (Koschny

and Grün, 2001). We note, that yield Y and micrometeoroid flux F_{imp} are rather uncertain.

Equation (4.6) can be readily solved to give a crude estimate for the optical depth of the moonlet population τ_m embedded in the ringlet, presuming known effective lifetime t_{life} and optical depth τ of the ringlet,

$$\tau_m \approx 11.8\,\tau \left(\frac{\mathrm{yr}}{t_{life}}\right). \tag{4.9}$$

From the normal optical depth τ_m we can derive an effective cross section $\sigma(r_m)$ and number density N_m/A, where N_m is the number of moonlets with radius r_m embedded in the ringlet (Eq. (4.4)). Moreover, we can then estimate the mass of the moonlet population, which again is assumed to have dominant source contribution.

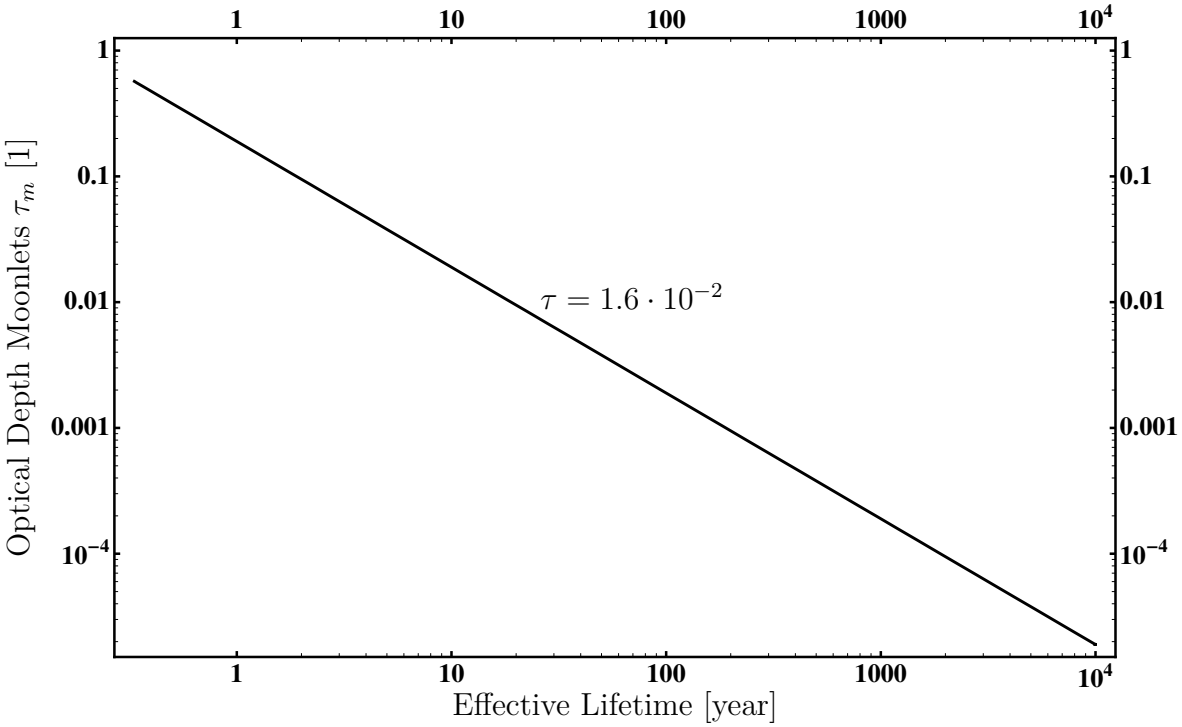

Figure 4.2 Optical depth of moonlets, that replenish the ringlet with material via micrometeoroid bombardment as a function of effective lifetime of the dust grains, evaluated for the central Encke gap ringlet. The normal optical depths has been derived by Porco et al. (2005), assuming mostly forward scatterers, i.e., small dust particles.

In Fig. 4.2 we plot relation (4.9), assuming an optical depth of the ringlet of $\tau = 1.6 \cdot 10^{-2}$, which has been given by Porco et al. (2005). The upper limit of the moonlets' optical depth is given by the heliotropic timescale, Eq. (3.28), which in the Encke gap results to $\tau_m \leq 0.6$ (Eq. (4.9)). This is very high, since the optical depth of the moonlets is expected to be smaller than the optical depth of the ringlet, measured by Porco et al. (2005). The lower limit is given by the maximal lifetime of the smallest dust grains. We use the sputtering timescale, which for the Saturnian system is roughly $10^{3\pm1}$ yr (Burns et al., 2001). Taking the upper estimate of 10^4 yr we find $\tau_m \geq 1.9 \cdot 10^{-5}$, which corresponds to a minimum of ≈ 300 moonlets with a radius of 500 m, or roughly $3 \cdot 10^{-2} M_{\mathrm{Pan}}$, needed to sustain the ringlet (Eq. (4.4)).

CHAPTER 5

Conclusion & Outlook

In the planar orbit-averaged picture we can give a solid understanding of the heliotropicity observed in some of Saturn's ringlets. Including three additional perturbation forces that lead to periodic eccentricity variations and precession of the longitude of pericenter, we qualitatively as well as quantitatively reproduce the "locked" orientation of the ringlet with respect to the Sun, neglecting any kinetic processes. The ringlet itself is modeled by superimposed annuli, which are created by the interaction of the three additional perturbation forces. We can constrain the minimal possible grain size that can possibly survive the heliotropic dynamics. We further can give a lower lifetime limit for particles, that form heliotropic ringlets. In the Encke gap we have chiefly $s_{\min} \approx 8.7$ microns, and lifetimes of at least 3 to 4 months.

The annulus model can fairly well reproduce observed eccentricities of the central ringlet, but has slight deficits in reproducing the observed confined ringlet-width. In Fig. 5.1 the left panel shows the Encke gap with its kinky and clumpy ringlets, the right panel gives a collage of the central Encke gap ringlet based on our annulus model and the A ring. Apparently, the ringlet-width is overestimated. This is due to neglected physics, which is a mixture of both, kinematic as well as kinetic mechanisms. The most promising kinematic mechanisms that may account for the ringlet-confinement as well as the kinky- and clumpiness are embedded moonlets and related stochastic scattering processes. Shepherding mechanisms likewise those of the F ring should also be considered in further investigations. Furthermore, azimuthal brightness variations as seen in the real world - also indicative for moonlets - cannot be described by our model.

From the kinetic point of view, we could identify several processes, that may serve as sinks and/or sources. We use a simple balance equation to model material gain and loss terms, whereas the loss term is black-boxed. Applying this model to the

central Encke gap ringlet provides us a relation between effective material lifetime and optical depth of embedded moonlets. Assuming lifetimes of 10^4 years, the mass of the embedded moonlet population should be at least of the order of $3 \cdot 10^{-2} M_{\mathrm{Pan}}$, in order to sustain the central Encke gap ringlet with dust material.

However, there is more to be included into a solid ringlet model. Starting from collisional dynamics of visco-elastic particles, including adhesion and gravity, ongoing gravitational scattering and other stochastic sources, a kinetic description of coagulation, restitution and fragmentation should also be taken into account. The magnitudes of potential sinks should be investigated further on, including erosion by means of UV-photon sputtering. This should yield a lifetime distribution, which is of crucial importance to explain the diverse structures seen in the Saturnian ringlets. All these

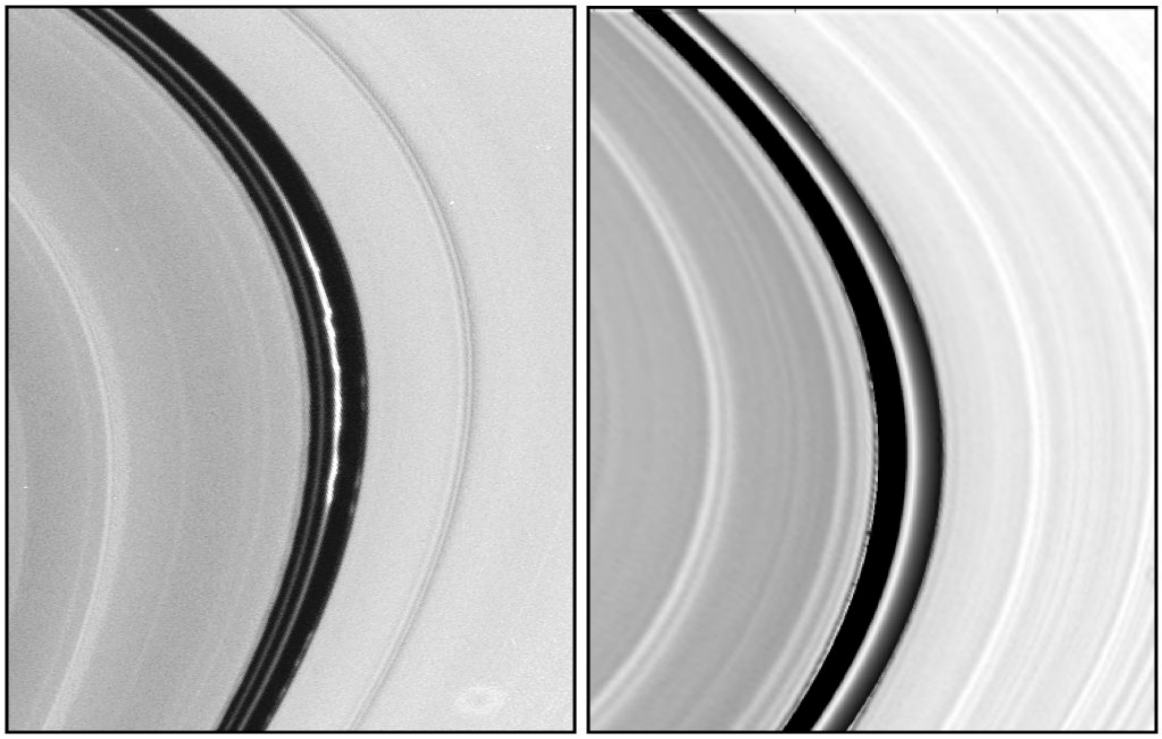

Figure 5.1 The left panel shows the Encke gap ringlets as seen in the real world. The right panel is a composition of a picture from the A ring and the theoretical modeled central ringlet, based on the annulus model, developed in this work. Credit: www.ciclops.org

items pinpoint milestones of future work in understanding the faint ringlets of Saturn. Finally, continuation and re-examination of Cassini data should provide hints for further investigative theoretical approaches, which might reveal new physics for these amazing structured, dusty ringlets in Saturn's ring system.

Bibliography

M. A. Ainslie. Occultation of B. D. +21°, 1714, by Saturn's ring, 1917 Feb. 9. *Monthly Notices Roy. Astron. Soc.*, 77:456–459, March 1917.

R. H. Brown, L. A. Soderblom, J. M. Soderblom, R. N. Clark, R. Jaumann, J. W. Barnes, C. Sotin, B. Buratti, K. H. Baines, and P. D. Nicholson. The identification of liquid ethane in titan's ontario lacus. *Nature*, 454(7204):607–610, 2008. URL `http://dx.doi.org/10.1038/nature07100`.

J. A. Burns, P. L. Lamy, and S. Soter. Radiation forces on small particles in the solar system. *Icarus*, 40:1–48, October 1979. doi: 10.1016/0019-1035(79)90050-2.

J. A. Burns, P. H Douglas, and M. R. Showalter. *Interplanetary Dust*. Interplanetary Dust, Edited by E. Grün, B.A.S. Gustafson, S. Dermott, and H. Fechtig. Astronomy and Astrophysics Library. 2001, 804 p., ISBN: 3-540-42067-3. Berlin: Springer, 2001., 2001.

J. W. Chamberlain. Depletion of satellite atoms in a collisionless exosphere by radiation pressure. *Icarus*, 39:286–294, August 1979. doi: 10.1016/0019-1035(79)90171-4.

J. N. Cuzzi, J. J. Lissauer, L. W. Esposito, J. B. Holberg, E. A. Marouf, G. L. Tyler, and A. Boishchot. Saturn's rings - Properties and processes. In R. Greenberg and A. Brahic, editors, *IAU Colloq. 75: Planetary Rings*, pages 73–199, 1984.

J. M. A. Danby. *Fundamental of Celestial Mechanics, 2nd ed.* Willmann-Bell, Richmond, 1988.

S. F. Dermott, C. D. Murray, and A. T. Sinclair. The narrow rings of jupiter, saturn and uranus. *Nature*, 284(5754):309–313, 1980.

N. Divine. Five populations of interplanetary meteoroids. *J. Geophys. Res.*, 98:17029–17048, September 1993. doi: 10.1029/0JGREA0000980000E9017029000001.

L. Dones. A recent cometary origin for Saturn's rings? *Icarus*, 92:194–203, August 1991. doi: 10.1016/0019-1035(91)90045-U.

C. Ferrari and A. Brahic. Arcs and clumps in the Encke division of Saturn's rings. *PSS*, 45:1051–1067, September 1997.

T. Gehrels, L. R. Baker, E. Beshore, C. Blenman, J. J. Burke, N. D. Castillo, B. Dacosta, J. Degewij, L. R. Doose, J. W. Fountain, J. Gotobed, C. E. Kenknight, R. Kingston, G. McLaughlin, R. McMillan, R. Murphy, P. H. Smith, C. P. Stoll, R. N. Strickland, M. G. Tomasko, M. P. Wijesinghe, D. L. Coffeen, and L. W. Esposito. Imaging photopolarimeter on Pioneer Saturn. *Science*, 207:434–439, January 1980.

C. K. Goertz. Dusty plasmas in the solar system. *Reviews of Geophysics*, 27:271–292, May 1989.

J. M. Hahn. Small Shepherd Satellites in Saturn's Encke Gap? In S. Mackwell and E. Stansbery, editors, *37th Annual Lunar and Planetary Science Conference*, volume 37 of *Lunar and Planetary Institute Conference Abstracts*, pages 1025–+, March 2006.

D. P. Hamilton. Motion of dust in a planetary magnetosphere - Orbit-averaged equations for oblateness, electromagnetic, and radiation forces with application to Saturn's E ring. *Icarus*, 101:244–264, February 1993. doi: 10.1006/icar.1993.1022.

D. P. Hamilton and A. V. Krivov. Circumplanetary Dust Dynamics: Effects of Solar Gravity, Radiation Pressure, Planetary Oblateness, and Electromagnetism. *Icarus*, 123:503–523, October 1996. doi: 10.1006/icar.1996.0175.

M. M. Hedman, J. A. Burns, M. S. Tiscareno, and C. C. Porco. The Heliotropic Rings of Saturn. In *AAS/Division for Planetary Sciences Meeting Abstracts*, volume 39 of *AAS/Division for Planetary Sciences Meeting Abstracts*, page 10.09, October 2007.

M. Henon and J.-M. Petit. Series expansion for encounter-type solutions of Hill's problem. *Celestial Mechanics*, 38:67–100, January 1986.

M. Horanyi. Charged Dust Dynamics in the Solar System. *Annual Review of Astronomy and Astrophysics*, 34:383–418, 1996. doi: 10.1146/annurev.astro.34.1.383.

M. Horanyi and J. A. Burns. Charged dust dynamics - Orbital resonance due to planetary shadows. *J. Geophys. Res.*, 96:19283–19289, November 1991.

M. Horanyi, J. A. Burns, and D. P. Hamilton. The dynamics of Saturn's E ring particles. *Icarus*, 97:248–259, June 1992. doi: 10.1016/0019-1035(92)90131-P.

S. Ida and K. Nakazawa. Collisional probability of planetesimals revolving in the solar gravitational field. III. *Astron. and Astrophys.*, 224:303–315, October 1989.

R. E. Johnson. Irradiation of solids: theory. In E. Bussoletti, G. Strazzulla, and P. Papali, editors, *Solid-State Astrophysics*, pages 129–+, 1991.

J. E. Keeler. The outer ring of Saturn. *Astron. J.*, 8:175–175, March 1889. doi: 10.1086/101150.

D. Koschny and E. Grün. Impacts into Ice-Silicate Mixtures: Crater Morphologies, Volumes, Depth-to-Diameter Ratios, and Yield. *Icarus*, 154:391–401, December 2001. doi: 10.1006/icar.2001.6707.

A. Krivov and A. Jurewicz. The ethereal dust envelopes of the Martian moons. *Planet. Space Sci.*, 47:45–56, February 1999.

A. Krivov, M. Sremčević, F. Spahn, V. V. Dikarev, and K. V. Kholshevnikov. Impact-generated dust clouds around planetary satellites: spherically symmetric case. *Planet. Space Sci.*, 51:251–269, March 2003.

H. Krüger, A. Krivov, D. P. Hamilton, and E. Grun. Discovery of an impact-generated dust cloud around Ganymede. *Nature*, 399:558–560, May 1999.

H. Krüger, A. V. Krivov, and E. Grün. A dust cloud of Ganymede maintained by hypervelocity impacts of interplanetary micrometeoroids. *Planet. Space Sci.*, 48: 1457–1471, December 2000.

J. J. Lissauer, S. W. Squyres, and W. K. Hartmann. Bombardment history of the Saturn system. *J. Geophys. Res.*, 93:13776–13804, November 1988.

M. Makuch, N. V. Brilliantov, M. Sremčević, F. Spahn, and A. V. Krivov. Stochastic circumplanetary dynamics of rotating non-spherical dust particles. *Planet. Space Sci.*, 54:855–870, August 2006. doi: 10.1016/j.pss.2006.05.006.

J. C. Maxwell. *On the Stability of the Motion of Saturn's Rings*. Macmillan and Company, Cambridge, 1859.

F. Mignard. Effects of radiation forces on dust particles in planetary rings. In R. Greenberg and A. Brahic, editors, *IAU Colloq. 75: Planetary Rings*, pages 333–366, 1984.

C. D. Murray and S. F. Dermott. *Solar System Dynamics*. Solar System Dynamics, by C.D. Murray and S.F. Dermott. ISBN 0521575974. Cambridge, UK: Cambridge University Press., February 2000.

C. D. Murray, K. Beurle, N. J. Cooper, M. W. Evans, G. A. Williams, and S. Charnoz. The determination of the structure of Saturn's F ring by nearby moonlets. *Nature*, 453:739–744, June 2008. doi: 10.1038/nature06999.

C. C. Porco, E. Baker, J. Barbara, K. Beurle, A. Brahic, J. A. Burns, S. Charnoz, N. Cooper, D. D. Dawson, A. D. Del Genio, T. Denk, L. Dones, U. Dyudina, M. W. Evans, B. Giese, K. Grazier, P. Helfenstein, A. P. Ingersoll, R. A. Jacobson, T. V. Johnson, A. McEwen, C. D. Murray, G. Neukum, W. M. Owen, J. Perry, T. Roatsch, J. Spitale, S. Squyres, P. Thomas, M. Tiscareno, E. Turtle, A. R. Vasavada, J. Veverka, R. Wagner, and R. West. Cassini Imaging Science: Initial Results on Saturn's Rings and Small Satellites. *Science*, 307(5713):1226–1236, 2005. doi: 10.1126/science.1108056. URL `http://www.sciencemag.org/cgi/content/abstract/307/5713/1226`.

H. J. Reitsema. Photometric confirmation of the Encke division in Saturn's ring A. *Nature*, 272:601–+, April 1978.

L. Schaffer and J. A. Burns. Lorentz resonances and the vertical structure of dusty rings - Analytical and numerical results. *Icarus*, 96:65–84, March 1992. doi: 10.1016/0019-1035(92)90006-S.

M. R. Showalter, J. N. Cuzzi, E. A. Marouf, and L. W. Esposito. Satellite 'wakes' and the orbit of the Encke Gap moonlet. *Icarus*, 66:297–323, May 1986. doi: 10.1016/0019-1035(86)90160-0.

M. R. Showalter, J. B. Pollack, M. E. Ockert, L. R. Doyle, and J. B. Dalton. A photometric study of Saturn's F Ring. *Icarus*, 100:394–411, December 1992. doi: 10.1016/0019-1035(92)90107-I.

F. Spahn. Scattering properties of a moonlet (satellite) embedded in a particle ring - Application to the rings of Saturn. *Icarus*, 71:69–77, July 1987. doi: 10.1016/0019-1035(87)90163-1.

F. Spahn and J. Schmidt. Planetary science: Saturn's bared mini-moons. *Nature*, 440:614–615, March 2006. doi: 10.1038/440614a.

F. Spahn and H. Sponholz. Existence of moonlets in Saturn's rings inferred from the optical depth profile. *Nature*, 339:607–+, June 1989. doi: 10.1038/339607a0.

F. Spahn and H.-J. Wiebicke. Long-term gravitational influence of moonlets in planetary rings. *Icarus*, 77:124–134, January 1989. doi: 10.1016/0019-1035(89)90012-2.

F. Spahn, K.-U. Thiessenhusen, J. E. Colwell, R. Srama, and E. Grün. Dynamics of dust ejected from Enceladus: Application to the Cassini dust detector. *J. Geophys. Res.*, 104:24111–24120, October 1999. doi: 10.1029/1999JE001031.

F. Spahn, A. V. Krivov, M. Sremčević, U. Schwarz, and J. Kurths. Stochastic forces in circumplanetary dust dynamics. *Journal of Geophysical Research (Planets)*, 108: 5021–+, April 2003. doi: 10.1029/2002JE001925.

F. Spahn, J. Schmidt, N. Albers, M. Hörning, M. Makuch, M. Seiß, S. Kempf, R. Srama, V. Dikarev, S. Helfert, G. Moragas-Klostermeyer, A. V. Krivov, M. Sremčević, A. J. Tuzzolino, T. Economou, and E. Grün. Cassini Dust Measurements at Enceladus and Implications for the Origin of the E Ring. *Science*, 311: 1416–1418, March 2006. doi: 10.1126/science.1121375.

M. Sremčević, J. Schmidt, H. Salo, M. Seiß, F. Spahn, and N. Albers. A belt of moonlets in Saturn's A ring. *Nature*, 449:1019–1021, October 2007. doi: 10.1038/nature06224.

G. Strazzulla and R. E. Johnson. Irradiation effects on comets and cometary debris. In R. L. Newburn, Jr., M. Neugebauer, and J. Rahe, editors, *IAU Colloq. 116: Comets in the post-Halley era*, volume 167 of *Astrophysics and Space Science Library*, pages 243–275, 1991.

M. S. Tiscareno, J. A. Burns, M. M. Hedman, C. C. Porco, J. W. Weiss, L. Dones, D. C. Richardson, and C. D. Murray. 100-metre-diameter moonlets in Saturn's A ring from observations of 'propeller' structures. *Nature*, 440:648–650, March 2006. doi: 10.1038/nature04581.

Declaration

I herewith declare that I have produced this paper without the prohibited assistance of third parties and without making use of aids other than those specified; notions taken over directly or indirectly from other sources have been identified as such. This paper has not previously been presented in identical or similar form to any other German or foreign examination board.

The thesis work was conducted under the supervision of Prof. Dr. Frank Spahn at the Universität Potsdam.

Robert J. Flassig
Potsdam, 22. September 2008

Deutsche Zusammenfassung

Im Sommer 2004 erreichte die Raumsonde Cassini Saturn, den zweitgrößten Planeten in unserem Sonnensystem. Seitdem wurden fantastische Entdeckungen von einer über 250 Wissenschaftler umfassenden internationalen Gemeinschaft gemacht, deren physikalische Erklärungen unser Verständnis der Welt enorm erweitert haben.

Die Saturnringe, welche aus losem, zumeist eisigem Staubmaterial bestehen, bieten außergewöhnlich viele Strukturen, welche räumlich und zeitlich mehr oder weniger stark variieren. Diese Eigenschaft resultiert aus einer Unzahl an zusätzlichen Kräften, welche die allgemein bekannte Kepler-Bewegung beeinflussen. So befinden sich mehrere Lücken, oder auch Teilungen, in den Ringen, welche schon in Voyager 1/2 Daten Anfang der achtziger Jahre gesehen wurden. Diese werden teilweise durch Resonanzen der Saturn Monde (z.B. innere Ringkante der Cassini Teilung und *Mimas*), aber auch durch Monde an sich (z.B. Keeler Teilung und *Daphnis*, Encke Teilung und *Pan*) über gravitative Wechselwirkungen erzeugt.

In diesen Ringteilungen befindet sich - mit Ausnahme von dem ein oder anderen feinen Staub-Ringlein - kein Material. Hedman et al. (2007) haben eine interessante Entdeckung gemacht. Einige dieser feinen Staub-Ringlein sind exzentrisch und halten eine besondere Orientierung zur Sonne aufrecht. Genauer, ihr Apozentrum ist in Richtung Sonne gerichtet, weshalb sie *heliotropische* Ringlein getauft wurden.

Für exzentrische Strukturen im Saturnsystem ist diese eingefrorene Orientierung ungewöhnlich. Normalerweise würde eine Präzession von exzentrischen Strukturen um Saturn auf einer Zeitskala von Monaten, deren Rate im Wesentlichen durch die Abplattung von Saturn bestimmt ist, erwartet werden.

In dieser Diplomarbeit untersuchen und erklären wir das außergewöhnlich heliotropische Verhalten qualitativ, sowie quantitativ mit Hilfe von Orbit gemittelten Störungsgleichungen. Dabei demonstrieren wir, dass ein Zusammenspiel von drei Störungskräften (Strahlungsdruck der Sonne, Abplattung der Pole vom Saturn, Lorentzkraft) periodisch gekoppelte Variationen von Orbitexzentrizität und Position des Perizentrums erzeugen, und im Ensembel einen exzentrischen Ring hervorbringen, dessen Apozen-

trum in Richtung Sonne zeigt.

Mit diesem Modell können wir gemessene Ringleinexzentrizitäten und -breiten in der Encke Teilung (Ferrari and Brahic, 1997, Hedman et al., 2007), unter Annahme gängiger Größenverteilungen (Divine, 1993, Krivov et al., 2003), sehr gut bzw. befriedigend reproduzieren. Die Ringleinbreiten werden um den Faktor 3 bis 10 überschätzt, was auf zusätzliche, nicht berücksichtigte Wechselwirkungen schließen läßt. Hier seien Teilchenstreunung an möglichen Moonlets (kleinere Monde) im Ringlein und Wechselwirkungen zwischen den Staubteilchen als zwei mögliche Ursachen genannt. Aufbauend auf dieser heliotropischen Dynamik können wir eine untere Grenze der Staubgrößenverteilung in der Encke Teilung ableiten, welche in eine Mindestlebenszeit für heliotropisches Ringleinmaterial übersetzt werden kann.

Motiviert durch die leicht überschätzen Ringleinbreiten, azimuthal unregelmäßigen Helligkeitsschwankungen (z.B. Ferrari and Brahic, 1997), früheren (Cuzzi et al., 1984, Spahn and Wiebicke, 1989, Spahn and Sponholz, 1989) und aktuellen Arbeiten (Murray et al., 2008), sowie der evidenten knickrigen Struktur des zentralen Encke Ringleins (siehe Titelbild, linke Seite), wenden wir zur Materialgenerierung das sog. Impact-Eject Szenario (Divine, 1993, Krüger et al., 1999) auf Moonlets an, welche an mit Sicherheit grenzender Wahrscheinlichkeit in dem Ringlein eingebettet sind.

Damit können wir ein einfaches kinetisches Modell basierend auf gemessenen Daten von Cassini (optische Tiefen, Porco et al., 2005) entwerfen. Jenes liefert, bei gegebener effektiver Lebenszeit der Teilchen im Ringlein in der Encke Teilung, eine dazu mindest nötige Quellmasse. Dabei räsonieren wir, dass Pan, welcher seine Bahn mit dem zentralen Ringlein der Encke Teilung teilt, eine untergeordnete Rolle als Materiallieferant spielt, und bestätigen somit die bisherigen Vermutungen von eingebetteten Moonlets im zentralen Ringlein der Encke Teilung. Jedoch zwingt Pan die als Materialquellen fungierenden Moonlets auf “Hufeisenbahnen”, was so das Ringlein radial begrenzt.

Des Weiteren vermuten wir, dass ein Großteil der Staubringlein auf diese Weise in einer stationären Balance zwischen Mikrometeoriten Erosion als Quelle und dynamischen Verlusten gehalten werden, welche erst durch die Existenz einer Moonlet-Population ermöglicht wird. Die Abschätzung der minimal nötigen Quellmasse liefert einen weiteren wichtigen Schritt in Richtung Antwort zu der Frage, in welcher Beziehung kleinere Monde wie Pan zu den sie umgebenden Ringlein stehen.

Zum Titelbild: Das Titelbild zeigt Saturns äußeren A Ring inklusive der Encke Teilung mit Haupt- und Nebenringlein (nur linkes Bild). Das recht Bild stellt eine Collage vom A Ring und dem Hauptringlein, welches durch das in dieser Diplomarbeit entwickelte Modell generiert wurde, dar. Im linken Bild, in der rechten unteren Ecke ist eine

Bildirritation zu erkennen. Diese ist auf ein Staubteilchen oder ähnliches zurückzuführen, welches womöglich auf die Kameralinse eingeschlagen ist.

Erklärung

Hiermit erläre ich, dass ich die vorliegende Arbeit mit dem Titel “Dusty Ringlets In Saturn’s Ring System” selbstständig und nur unter Verwendung der angegebenen Hilfsmittel und Literatur angefertigt habe.

Diese Arbeit wurde an keiner anderen Hochschule eingereicht

Robert J. Flassig
Potsdam, 22. September 2008